Dyke emplacement and crustal structure within a continental large igneous province, northern Barents Sea

ALEXANDER MINAKOV[1,2]*, VIKTORIYA YARUSHINA[3], JAN INGE FALEIDE[1], NATALIYA KRUPNOVA[4], TAMARA SAKOULINA[4], NIKOLAY DERGUNOV[4] & VLADIMIR GLEBOVSKY[5]

[1]*Centre for Earth Evolution and Dynamics, University of Oslo, NO-0315 Oslo, Norway*

[2]*VISTA, Norwegian Academy of Science and Letters, N-0271 Oslo, Norway*

[3]*Institute for Energy Technology, NO-2007 Kjeller, Norway*

[4]*JSC Sevmorgeo Rosnedra, 198095 St Petersburg, Russia*

[5]*VNIIOkeangeologia, 190121 St Petersburg, Russia*

**Correspondence: alexander.minakov@geo.uio.no*

Abstract: We perform an integrated analysis of magnetic anomalies, multichannel seismic and wide-angle seismic data across an Early Cretaceous continental large igneous province in the northern Barents Sea region. Our data show that the high-frequency and high-amplitude magnetic anomalies in this region are spatially correlated with dykes and sills observed onshore. The dykes are grouped into two conjugate swarms striking oblique to the northern Barents Sea passive margin in the regions of eastern Svalbard and Franz Josef Land, respectively. The multichannel seismic data east of Svalbard and south of Franz Josef Land indicate the presence of sills at different stratigraphic levels. The most abundant population of sills is observed in the Triassic successions of the East Barents Sea Basin. We observe near-vertical seismic column-like anomalies that cut across the entire sedimentary cover. We interpret these structures as magmatic feeder channels or dykes. In addition, the compressional seismic velocity model locally indicates near-vertical, positive finger-shaped velocity anomalies (10–15 km wide) that extend to mid-crustal depths (15–20 km) and possibly deeper. The crustal structure does not include magmatic underplating and shows no regional crustal thinning, suggesting a localized (dyking, channelized flow) rather than a pervasive mode of magma emplacement. We suggest that most of the crustal extension was taken up by brittle–plastic dilatation in shear bands. We interpret the geometry of dykes in the horizontal plane in terms of the palaeo-stress regime using a model of a thick elastoplastic plate containing a circular hole (at the plume location) and subject to combined pure shear and pressure loads. The geometry of dykes in the northern Barents Sea and Arctic Canada can be predicted by the pattern of dilatant plastic shear bands obtained in our numerical experiments assuming boundary conditions consistent with a combination of extension in the Amerasia Basin sub-parallel to the northern Barents Sea margin and a mild compression nearly orthogonal to the margin. The approach has implications for palaeo-stress analysis using the geometry of dyke swarms.

Supplementary material: Details on traveltime tomography model: Resolution tests, traveltime information and ray coverage are available at https://doi.org/10.6084/m9.figshare.c.3783542

Many continental large igneous provinces (LIPs) have been formed throughout Earth history (Coffin & Eldholm 1994; Ernst 2014). A typical LIP event is associated with the eruption of $>10^6$ km^3 of basalts. This massive eruption of flood basalts and the corresponding intrusive components are attributed to a temperature and melting anomaly in the mantle resulting from plumes (Richards *et al.* 1989; White & McKenzie 1995). The main eruptive phase of flood basalts is geologically short and typically lasts 1–5 myr (Jerram & Widdowson 2005; Svensen *et al.* 2012). LIPs are closely linked to continental break-up (Buiter & Torsvik 2014). The effect of magmatic weakening and magma-assisted break-up is pronounced in the central Atlantic (Hames *et al.* 2000) and on the NE Atlantic margins (Eldholm & Grue 1994), the East African rift (Ebinger & Casey 2001; Buck 2006; Kendall *et al.* 2005) and the India–Seychelles margins (Minshull *et al.* 2008).

Giant radiating dyke swarms are often associated with LIPs and can be used as markers to reconstruct the pre-break-up position of the continents (Ernst *et al.* 2013). The orientation of dykes can also be used to infer the palaeo-stress regime on pre-break-up continental margins (Hou *et al.* 2010).

From: Pease, V. & Coakley, B. (eds) *Circum-Arctic Lithosphere Evolution*. Geological Society, London, Special Publications, **460**, https://doi.org/10.1144/SP460.4

However, existing models for the formation of giant dyke swarms are partly based on Venusian analogues (associated with coronae structures) because entire palaeo-structures are less likely to be preserved on Earth due to erosion and plate tectonics (McKenzie *et al.* 1992). The lack of structural constraints and the complex geometry of giant dyke swarms has promoted debates on the physical mechanisms behind their formation and the part played by mantle plumes (e.g. McHone *et al.* 2005). This paper addresses the mechanical aspects of the genesis and geometry of giant dyke swarms and the key role of the rheological behaviour of the lithosphere when affected by a mantle plume.

A giant radiating dyke swarm was identified in the circum-Arctic continental shelves of the Arctic region by Buchan & Ernst (2006). This supported the existence of the High Arctic LIP-related magmatic event (Lawver & Müller 1994; Tarduno 1998; Maher 2001) previously inferred from a number of structural and lithological observations, including the geochemistry of basalts (Bailey & Rasmussen 1997; Ntaflos & Richter 2003; Drachev & Saunders 2006). The later analysis of detailed aeromagnetic data (Minakov *et al.* 2012*a*; Døssing *et al.* 2013) and analysis of multichannel and wide-angle seismic profiles (Grogan *et al.* 2000; Minakov *et al.* 2012*a*; Polteau *et al.* 2016) suggested a significant intrusive component in the High Arctic LIP in the Barents Sea.

The lack of vegetation and perfect exposure in the islands of the northern Barents Sea region allows a unique correlation of geophysical data and onshore geology. Most dykes in Franz Josef Land are near-vertical with a thickness that ranges between 2 and 30 m, but this may increase locally to >100 m (Dibner 1998). Basalt flows are typically 2–70 m thick, locally up to 100 m, with a total thickness of 200–350 m. From a geochemical point of view, two major groups have been identified: low-potassium tholeiitic basalts and andesitic basalts (Ntaflos & Richter 2003; Dibner 1998).

Corfu *et al.* (2013) determined the crystallization ages of mafic sills in Svalbard and Franz Josef Land using U–Pb methods on different minerals. The ages obtained suggest rapid magma emplacement, in agreement with previous studies of other LIPs (Hames *et al.* 2000; Svensen *et al.* 2012). Their results indicate ages of *c.* 124 and 122 Ma (with an accuracy within 1 myr) for the sills in Svalbard and Franz Josef Land, respectively. $^{40}K/^{40}Ar$ and $^{40}Ar/^{39}Ar$ data (Piskarev *et al.* 2009; Nejbert *et al.* 2011; Shipilov & Karyakin 2011) indicate a much larger spread of ages (*c.* 200–90 Ma) with an uncertainty of some determinations of up to $\pm$29 myr (Shipilov & Karyakin 2011). The interpretation of these data in terms of the timing of dyke emplacement is not straightforward. Isotopic geochronology studies in other continental LIPs have shown that the U–Pb dating technique generally gives a better constraint on the crystallization age of mafic intrusions than the K–Ar and Ar–Ar systems, which can be strongly affected by a complex thermal history, extraneous Ar, recoil loss, uncertainties in the ages of standards and other factors (e.g. Svensen *et al.* 2012).

In this study, we reserve the term High Arctic LIP for the main intrusive phase of magmatism, postulated to be a result of the plume–lithosphere interaction that initiated continental break-up of the Arctic continental lithosphere (Lawver & Müller 1994; Drachev & Saunders 2006). We assume that the younger Late Cretaceous magmatism (100–70 Ma) in the west Arctic region (e.g. Tegner *et al.* 2011) may be related to lithosphere rifting. The proposed view is documented by a large dataset of geological and geophysical information in the Barents Sea. We reprocess and analyse magnetic data and seismic refraction and multichannel seismic reflection data covering the dyke swarms in the northern Barents Sea. These data show that there was no large amount of extension/rifting of continental lithosphere before the start of magmatism in the Barents Sea. The lack of Cenozoic faults or magmatism in the northern Barents Sea (Minakov *et al.* 2012*b*) makes it possible to infer the lithospheric stresses associated with the emplacement of the Early Cretaceous mafic dyke swarms by matching their geometry with the results of mechanical modelling. The magnetic data show a radiating pattern of dykes cross-cutting the Barents Sea shelf (Figs 1 & 2). We use these data as a rationale to discuss a possible mechanism for dyke emplacement and to predict the stress pattern related to early stages of the evolution of the Amerasia Basin. We briefly review the existing models for dyke geometry, which are primarily based on elastic models. We draw attention to the phenomenon of dilatant plastic shear bands, which, we believe, controlled the geometry of dykes.

Geophysical data and processing

Seismic data

Seismic data were acquired SE of Kong Karls Land by the University of Bergen (Minakov *et al.* 2012*a*) and in the eastern Barents Sea by the Joint Stock Company (JSC) Sevmorgeo (Ivanova *et al.* 2011; Sakoulina *et al.* 2015). These data were then combined to produce a composite deep seismic transect across the northern Barents Sea (Fig. 1). The western part (ESVA) consists of a 170 km long profile acquired in 2008, along which 14 ocean bottom seismometers were deployed. The acoustic source consisted of four equal-sized airguns with a total

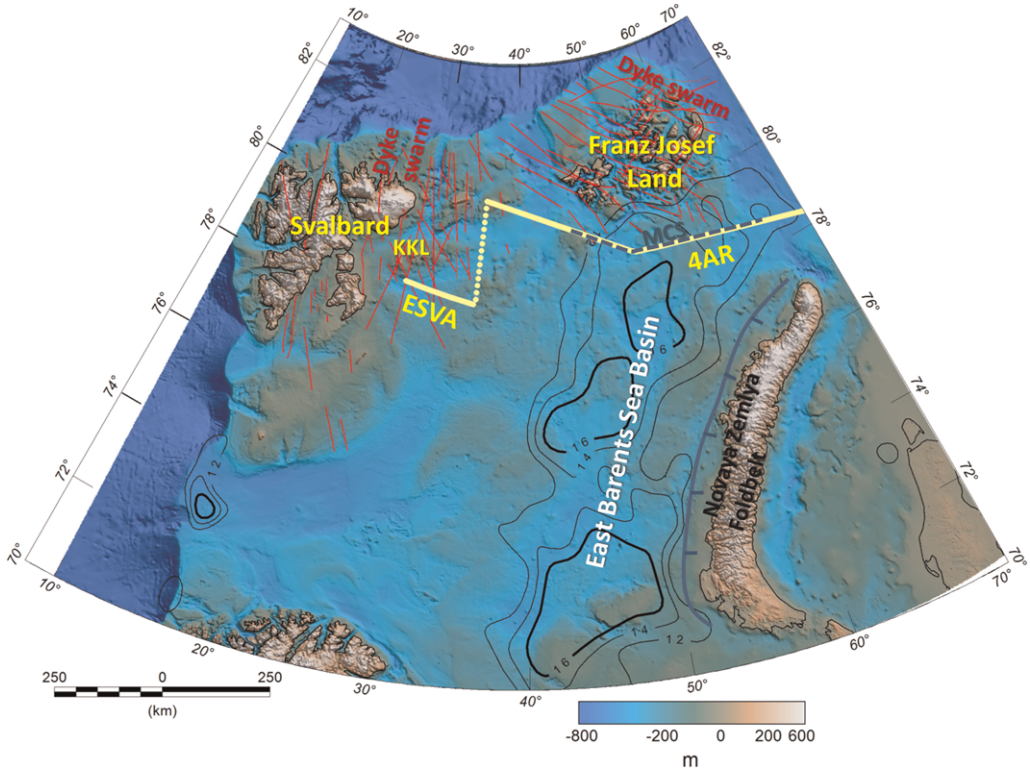

Fig. 1. Bathymetry of the Barents Sea region. Red lines are the axes of magnetic anomalies interpreted as Early Cretaceous dolerite dykes. A composite seismic transect (ESVA–4AR) crosses the giant radiating dyke swarms in the northern Barents Sea. The East Barents Sea Basin is shown using contours of depth to top-crystalline-basement from Klitzke *et al.* (2015). The location of the crustal-scale transect in Figure 3 is shown by the yellow line. The location of the seismic profile in Figure 4 is shown by the dashed grey line. The SRTM15_PLUS (2015 release) global topography grid (Becker *et al.* 2009; Smith & Sandwell 1997) is used, which includes the bathymetry from the International Bathymetric Chart of the Arctic Ocean (Jakobsson *et al.* 2012) for the Arctic region. KKL, Kong Karls Land; MCS, multichannel seismic reflection profile.

volume of about 80 l that were fired every 200 m. The processing of these data is described in Minakov *et al.* (2012*a*). The eastern part of the transect (4-AR) consists of a combined wide-angle and multichannel seismic (MCS) reflection profile, acquired in 2005–6, which crosses the northern Barents Sea and the northernmost part of the Novaya Zemlya fold belt (Ivanova *et al.* 2011; Sakoulina *et al.* 2015). The profile was acquired in four legs (each 240–500 km long) and has a total length of 1370 km. Only part of the profile (140–1000 km) is presented here. The ocean bottom seismic stations were deployed at 10 km intervals along 4-AR. The acoustic source consisted of a powerful single airgun with a chamber volume of about 120 l. The shot interval was 250 m. The data processing has been previously described in Ivanova *et al.* (2011) and Sakoulina *et al.* (2015).

We remodelled the western part of the 4-AR transect using a combined reflection and refraction tomography method (Hobro 1999; Hobro *et al.* 2003). The profile was processed separately for the two segments: the WNW–ESE part (140–500 km) and the east–west part (500–1000 km). The first arrivals and Moho-reflected travel times were picked after standard processing had been applied to the recorded data, including bandpass filtering, deconvolution and the normalization of amplitudes by Ivanova *et al.* (2011) and Sakoulina *et al.* (2015).

We performed travel-time tomography using the JIVE3D code (Hobro 1999; Hobro *et al.* 2003). Using this approach, the travel-time misfit function was optimized together with smoothness constraints to find a P-wave velocity model. A one-dimensional starting model was constructed using previously

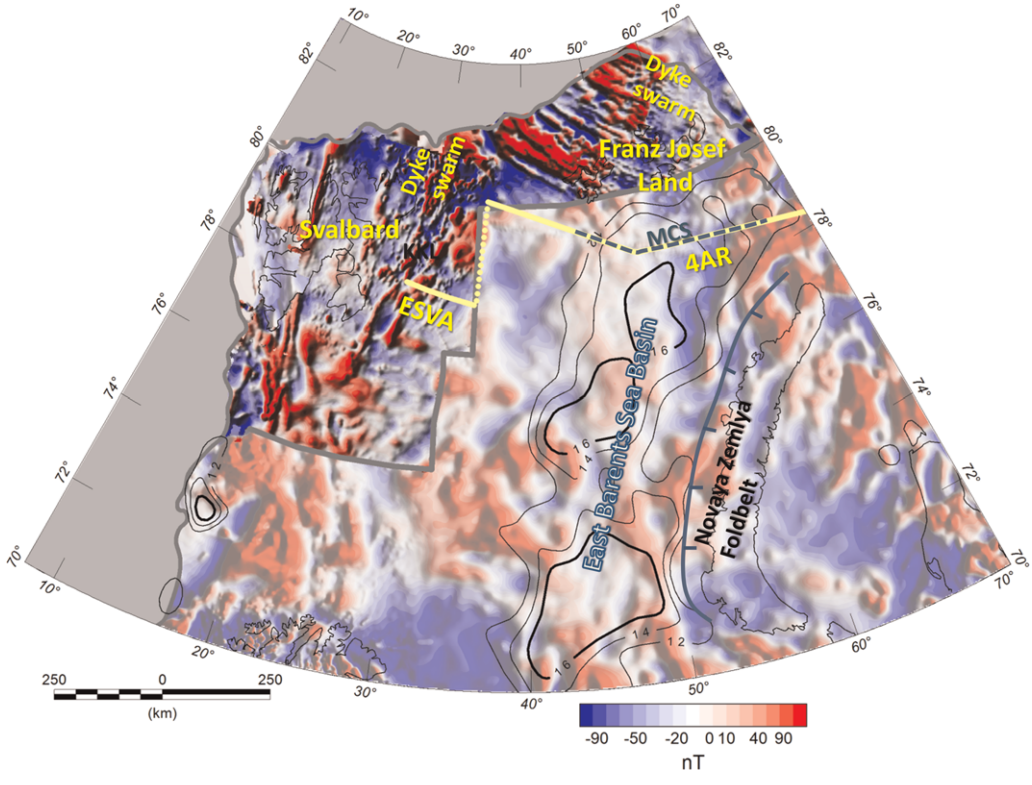

Fig. 2. Magnetic anomalies of the Barents Sea region. A composite seismic transect (ESVA–4AR) crosses the giant radiating dyke swarms in the northern Barents Sea. The East Barents Sea Basin is shown using contours of depth to top-crystalline-basement from Klitzke *et al.* (2015). The higher resolution grids with a cell size of 2 km are highlighted in more saturated colours. The location of the crustal-scale transect in Figure 3 is shown by the yellow line. The location of the seismic profile in Figure 4 is shown by the dashed grey line. KKL, Kong Karls Land; MCS, multichannel seismic reflection profile.

published velocity models in the northern Barents Sea (Minakov *et al.* 2012*a*; Ivanova *et al.* 2011; Sakoulina *et al.* 2015). The forward problem solution was based on a ray perturbation method adopted from Farra & Madariaga (1987). The optimization problem was solved using the iterative LSQR method (Paige & Saunders 1982). We used 30 non-linear iterations to update the initial starting model. The uncertainty of picking was set to 100 ms beyond 30 km offset and 70 ms at closer distances. The final χ^2 value was *c.* 2.3 for the WNW–ESE segment and *c.* 1.3 for the east–west segment. We attribute the increase in the χ^2 value for the WNW–ESE segment to a complex three-dimensional velocity structure. We show the velocity model resulting from our tomographic inversion of the Pg and PmP phases in Figure 3b, c, together with the velocity model of Sakoulina *et al.* (2015), which is based on forward modelling of all the interpreted phases, including the secondary arrivals. The two models are in general agreement apart from minor discrepancies in the configuration of Moho. The details on model resolution, ray coverage and travel misfit can be found in Supplementary Material.

The MCS survey along the 4-AR profile (Figs 4 & 5) was carried out by JSC Sevmorneftegeofizika in 2005 onboard RV *Akademik Lazarev*. The airgun source consisted of 4258 in^3 (69.8 l) BOLT 1900 airguns. The SeaMUX 2000 seismic streamer was used as a receiver. The main acquisition parameters are provided in Table 1. The seismic data along the 4-AR profile were processed by JSC Sevmorgeo. The initial processing was performed using FOCUS software (Paradigm Geophysical) and is presented in Ivanova *et al.* (2011).

In this work, the data were reprocessed to eliminate surface-related multiple reflections. The re-processing of the 4-AR MCS data was performed using FOCUS and GeoDepth software (Paradigm Geophysical). The processing sequence included

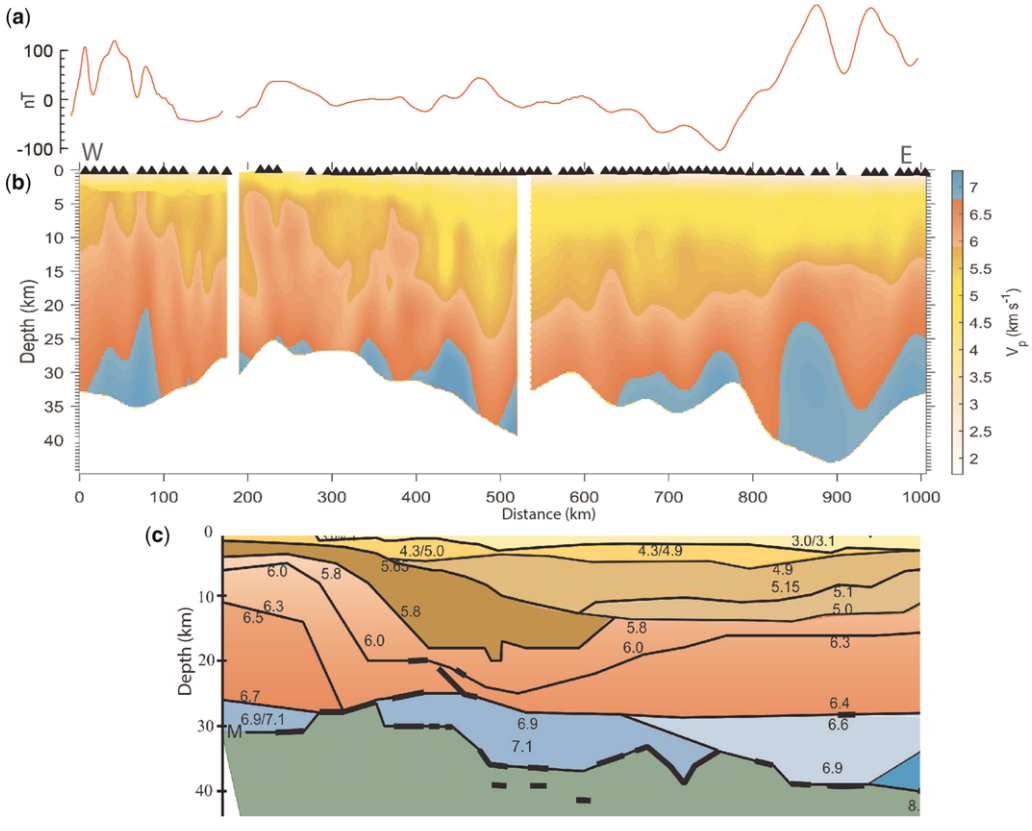

Fig. 3. P-wave velocity model along the wide-angle profiles ESVA and 4AR. (**a**) Magnetic anomalies extracted along the crustal transect. (**b**) Results of refraction and reflection tomography in this study. Location of ocean bottom stations is shown by black triangles. (**c**) Results of forward modelling by Sakoulina *et al.* (2015). The velocity models do not show underplating, indicating predominantly localized (dykes, channelized magma flow) rather than pervasive magmatic transport associated with the High Arctic large igneous province in the northern Barents Sea. We suggest that most of the crustal extension was taken up by brittle–plastic dilatation in shear bands.

bandpass filtering, multiple removal by surface-related multiple elimination, velocity analysis, geometrical spreading amplitude correction, τ–p deconvolution, multiple suppression using Radon transform, spectral equalization and broadening of the spectrum.

The final processing step consisted of seismic migration applied to the shot data in the time domain. We applied Kirchhoff pre-stack time migration using average (RMS) velocities. In addition, F–X and time-dependent deconvolution were applied to migrated seismic sections.

Magnetic anomalies

We compiled a magnetic anomaly map for the northern Barents Sea region (Fig. 2) including a 5 × 5 km grid extracted from the circum-Arctic CAMP compilation (Gaina *et al.* 2011) and 2 × 2 km grids for the Svalbard and Franz Josef Land regions. The aerogeophysical survey over Franz Josef Land was carried out by the Polar Marine Geological Expedition in 1997 and 1998–2000. The results of the processing and interpretation of trackline data were presented in Verba *et al.* (2004), Glebovsky *et al.* (2006*a*, *b*) and Minakov *et al.* (2012*b*). The magnetic data over the Svalbard region were acquired by Sevmorgeo–Polar Marine Geological Expedition, the TGS-NOPEC Geophysical Company and the Norwegian Geological Survey in 1989–91. The results of data processing and interpretation south and east of Svalbard can be found in Skilbrei (1991), Skilbrei (1992) and Olesen *et al.* (2010). The specifications of the aeromagnetic data are given in Table 2.

The profile aeromagnetic data over Franz Josef Land were reprocessed by VNIIOkeangeologia, including more accurate levelling procedures. The

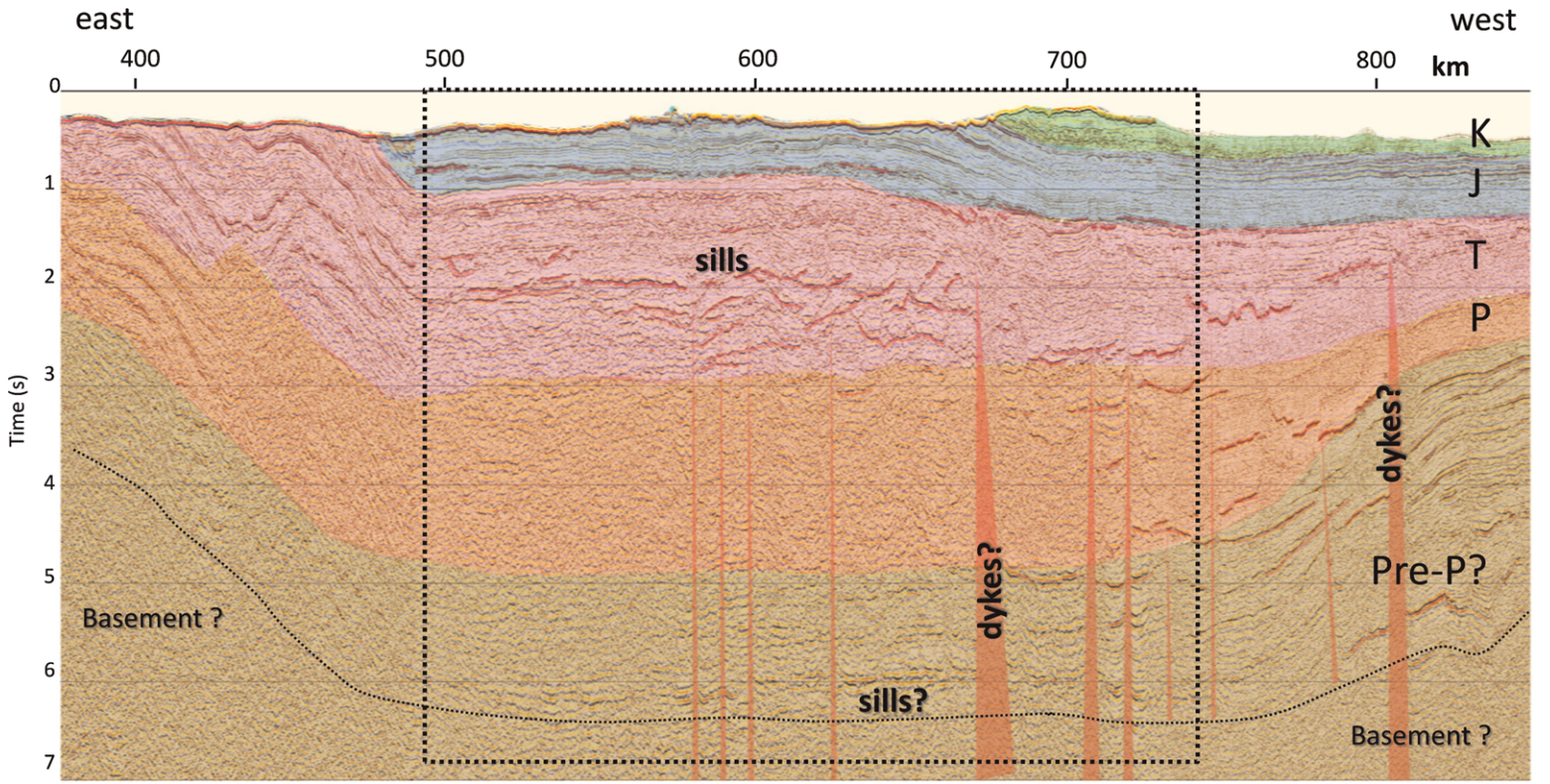

Fig. 4. Multichannel seismic data across the northern East Barents Basin, Profile 4-AR (380–850 km); see Figures 1 and 2 for location. The interpretation of seismic stratigraphic units follows Ivanova *et al.* (2011). The interpreted stratigraphic units are: K, Cretaceous; J, Jurassic; T, Triassic; P, Permian. Possible dykes/feeders and sills are highlighted. A number of sills are identified in Triassic strata; some sills are also inferred at deeper levels, particularly at the sediment–crystalline basement interface. Most dyke-like anomalies pinch out in Triassic strata. The location of the data subset shown in Figure 5 is indicated by the dashed box.

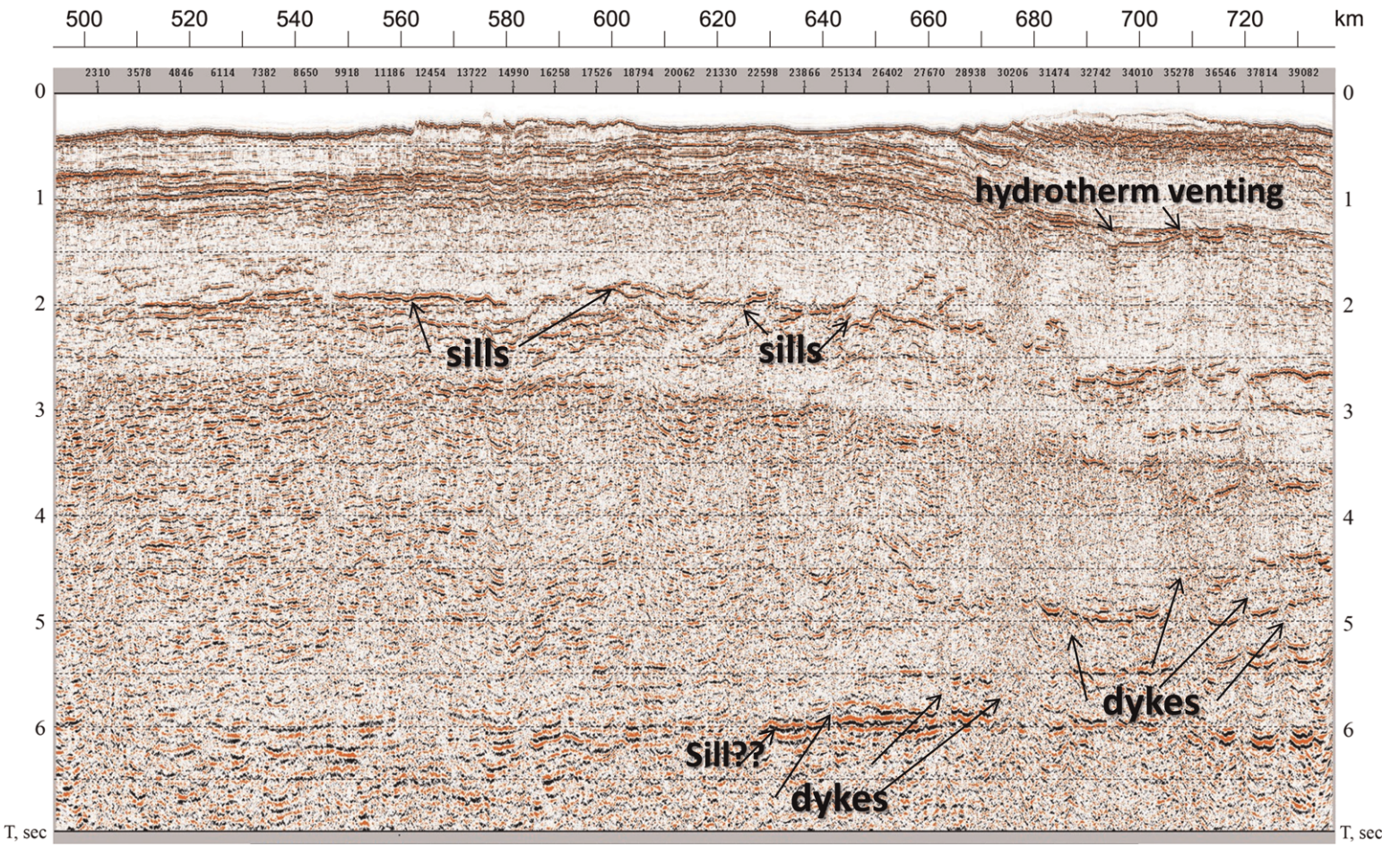

Fig. 5. Zoomed uninterpreted multichannel seismic section showing mafic intrusive complexes within the northern East Barents Sea Basin.

Table 1. *Acquisition parameters for the multichannel seismic reflection data*

Parameter	Value
Shot point interval	37.5 m
Source depth	10 m
Streamer length	6000 m
Number of recording channels	480
Group interval	12.5 m
Nominal fold	80
Record length	12 s
Sampling rate	2 ms

additional processing included the adjustment of the regional trends in the data. We used a 500 km Butterworth low-pass filter to extract a regional trend of magnetic anomalies from the CAMP grid. The corresponding long-wavelength component was removed from the local grids for the Svalbard and Franz Josef Land areas and replaced by the trend derived from the CAMP grid.

Geological interpretations

We present here an integrated interpretation of the seismic and magnetic data within the northern Barents Sea region with an emphasis on the geometry and distribution of mafic intrusions. The study region consists of the Kong Karls Land platform (a Permian–Carboniferous carbonate platform overlain by 1–4 km of Mesozoic sediments; Grogan *et al.* 1999) and the ultra-deep East Barents Sea sedimentary basin in the east (Drachev *et al.* 2010), which stretches along the Novaya Zemlya islands (Fig. 1). The northern part of this basin is sometimes considered as a separate unit: the North Barents Basin (e.g. Ivanova *et al.* 2011). The basin contains Upper Devonian–Cretaceous sediments with major subsidence during Permian–Triassic times (Drachev *et al.* 2010; Gac *et al.* 2012). Onshore western Franz Josef Land, a well penetrated a mainly Triassic section (including a thin layer of Carboniferous sediments) overlain by Barremian to Albian basalts interbedded with coal-bearing sediments (Dibner *et al.* 1992). The well penetrated a Vendian (Ediacaran) metamorphic basement at about *c.* 2 km depth (Dibner *et al.* 1992). In the eastern part of the archipelago, two wells were terminated at *c.* 3.5 km in siliciclastic Middle Triassic (Anisian) strata. The stratigraphic interpretation of the seismic section in Figure 3 generally follows Ivanova *et al.* (2011).

Dykes

As revealed by the aeromagnetic data (Fig. 2), the dykes in the northern Barents Sea can be grouped into two regional swarms running oblique to the passive margin: the Franz Josef Land and the Svalbard dyke swarms, respectively. The first swarm penetrates the existing structural grain of Franz Josef Land and the region north of Novaya Zemlya. In the west Svalbard region, the dykes probably follow Caledonian (and older) faults (Ritzmann & Faleide 2007; Breivik *et al.* 2005; Gernigon & Brönner 2012). The Carboniferous graben and associated faults (Faleide *et al.* 2008) may also facilitate magma migration at shallower levels south of Kong Karls Land (Minakov *et al.* 2012*a*). North of Kong Karls Land, the dykes cut pre-existing basement structures inferred from geophysical data. Most of the dykes in Figures 1 and 2 are 30–90° off the boundaries of basement blocks and zones of weakness identified by Marello *et al.* (2013). Another interesting observation is that a number of dykes within the Svalbard swarm intersect.

The NW part of the Franz Josef Land archipelago is covered by plateau basalts that correspond to a broad magnetic high (Dibner 1998). The dykes intruding the sedimentary cover (and locally

Table 2. *Specifications of aeromagnetic data*

Survey	Parameter	Value
Franz Josef Land		
Polar Marine Geological Expedition (1997, 1998–2000)	Trackline spacing	5–10 km
	RMS	5 nT
	Flight altitude	500–800 m
	Direction of tracklines	North–south
Svalbard		
Sevmorgeo–Polar Marine Geological Expedition, TGS-NOPEC, Norwegian Geological Survey (1989–91)	Trackline spacing	4–8 km
	RMS	6–9 nT
	Flight altitude	250, 900, 1550 m
	Direction of tracklines	East–west

cutting the extrusive rocks) correlate with positive high-frequency and high-amplitude magnetic anomalies. We assume that dyke emplacement during a normal polarity period and a steep orientation of the natural remanent magnetization (Abashev *et al.* 2015) allows for this direct correlation.

In the multichannel seismic data (Figs 4 & 5), the dykes can be identified as sub-vertical discontinuities that can be traced below 6–7 s (13–15 km depth) and pinch out at about 2 s (*c.* 3 km depth), as was shown previously by Khlebnikov *et al.* (2011). The sills in the East Barents Basin are often spatially associated with these vertical zones of disrupting seismic signatures. On the seismic section, these vertical features are wider at the top-crystalline-basement and pinch out at the average depth of sills. The seismic horizons bend upwards in the vicinity of these anomalies, which may be related to ascending magma and/or fluids. The dyke anomalies are best imaged on the eastern flank of the East Barents Basin (SE of Franz Josef Land). In the central part of the basin the interpretation is more complicated below the high-velocity sill complex (Polteau *et al.* 2016). Here the dyke anomalies are thinner and occur locally, as seen in a zoomed subset of the uninterpreted seismic section (Fig. 5). We acknowledge that the interpretation of these features is not unique. For example, a localized flow of metamorphic fluids penetrating the crystalline basement could also result in a similar pattern.

Sills and lava flows

In the MCS data (Figs 4 & 5), we identify sill intrusions in the East Barents Sea Basin based on the following criteria: a high (positive) acoustic impedance contrast; unconformable relations with the host sedimentary layers; and the saucer-shaped geometry of reflectors (Figs 4 & 5). In seismic sections, these sub-horizontal anomalies are most clearly observed in the Middle Triassic strata. Subvolcanic intrusive and extrusive mafic rocks are also assumed in the lowermost Cretaceous strata based on the MCS data. Similar magmatic rocks are observed within the Upper Jurassic Agardfjellet Formation in the Kong Karls Land platform (Grogan *et al.* 2000).

Most of the saucer-shaped sill intrusions visible on seismic data are within Triassic organic-rich siliciclastic rocks in the central part of the profile (Figs 4 & 5). A possible large sub-horizontal sill complex (lateral extent 100–200 km) can be identified near the top-basement at *c.* 6 s (about 13 km depth) (Figs 4 & 5). This interpretation is supported by two sills (150 and 400 m thick) in the Lower Carboniferous strata and a thick mafic sill at the top-basement (Carboniferous–Ediacaran transition) penetrated by a borehole in western Franz Josef Land (Dibner 1998, p. 126).

The average thickness of sills observed onshore Franz Josef Land in both boreholes and outcrops varies in the range 20–100 m. A similar thickness of sills is reported for the Svalbard region (Senger *et al.* 2014*a*). Metamorphic aureoles are observed within a few tens of metres of the dyke contact in Franz Josef Land (Dibner *et al.* 1992). The thickness of the contact aureoles in the host sediments reported for Spitsbergen is one-and-a-half to two times larger than the thickness of the sills (Senger *et al.* 2014*b*).

Possible hydrothermal vent complexes are identified at about 1.5–1.8 s (1.5–2 km depth) in the eastern flank of the basin, just above the dyke anomalies (Fig. 5). A northerly location of the major volcanic activity is suggested by the presence of lava flows on Franz Josef Land (particularly abundant in the western part of the archipelago) and on Kong Karls Land (east of Svalbard). Sill intrusions in the north are generally shallower (and in younger stratigraphic intervals) than in the southern part of the East Barents Basin (Shipilov & Karyakin 2011), possibly indicating a northwards increase in magma volume and pressure.

Structure of crystalline crust

The crustal P-wave velocity model (Fig. 3) indicates that the northern part of the East Barents Sea Basin is confined between two higher velocity domains (profile distances 0–400 and 750–1000 km, respectively). The thicker crust in the east is probably related to the northernmost tip of the Novaya Zemlya fold–thrust belt, which links to the Taimyr fold belt in the east (Drachev *et al.* 2010). The western part of the profile can be interpreted as a Caledonian crystalline basement modified by mafic intrusions (at a profile distance of 0–300 km). The northern East Barents Sea Basin is characterized by lower velocities in the crystalline crust (5.8–7.1 km s^{-1}).

The Moho depth within the basin varies between 29 and 35 km. It increases to the east and approaches >40 km at the northern tip of the Novaya Zemlya fold–thrust belt. A slight increase in crustal thickness east of Svalbard may be the result of mafic intrusions in the lower crust. Crustal thickening and/or buckling as a result of the Eocene Eurekan/Svalbard Orogeny cannot be excluded. However, some observations suggest that the formation of the fold–thrust belt was associated with a thin-skin deformation restricted to western Svalbard (e.g. Leever *et al.* 2011). Thus it appears from the lower crustal velocities that the amount of possible underplated intrusive material or magmatic lower crust is limited. In addition, the velocity model across the northern Barents Sea does not indicate

significant stretching of the crust associated with the LIP magmatism, assuming 35 km as an average thickness of the continental crust. The bulk velocities in the crystalline crust are in the range 6.0–7.0 km s^{-1}, which is much lower than is typical for a mafic igneous lower crust (Ridley & Richards 2010). This indicates that the transport of magma in the crust was localized rather than pervasive (underplating). Although these two processes are not mutually exclusive, we conclude that most of the High Arctic LIP intrusions in the northern Barents Sea were emplaced by localized magma transport, such as dyking and/or channelized magmatic flow.

The pattern of P-wave velocity anomalies (Fig. 3b) is characterized by the presence of high-velocity finger-shaped anomalies, which have previously been interpreted east of Svalbard as parts of a Lower Cretaceous magmatic feeder system (Minakov *et al.* 2012*a*). The high-velocity anomalies south of Kong Karls Land (up to 10% with respect to the one-dimensional background velocity model) are spatially correlated with the sills and dykes at shallower levels. The dyke-like anomalies in the multichannel data in Figures 4 and 5 are sometimes spatially correlated with higher compressional velocities in the crystalline crust. A 2–3 km increase in the Moho depth is observed beneath this type of velocity anomaly in the western part of the profile (Fig. 3; 0–100 km).

The architecture of the crystalline crust is characterized by the basement highs and lows, which correspond to gentle domes and sinks in the structure of the sediments above. The reflection seismic data indicate that the Franz Josef Land region already represented a structural high in Mesozoic times, whereas Cenozoic uplift and erosion (Henriksen *et al.* 2011; Minakov *et al.* 2012*b*) emphasized the present day topography in the NE Barents Sea.

Conceptual model

We summarize the geological and geophysical information in the form of the conceptual model in Figure 6. The model includes a magmatic source

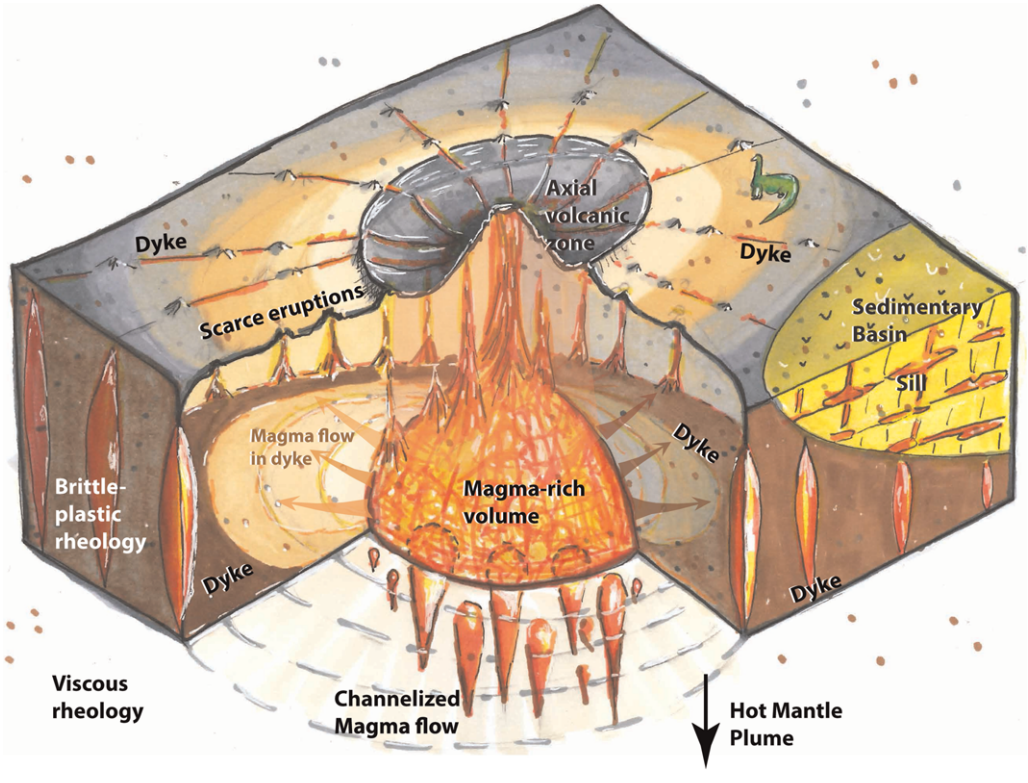

Fig. 6. 'Geofantasy' on dyke emplacement and crustal structure within a continental large igneous province. Buoyancy-driven channelized magmatic flow originates in the lowermost lithosphere, where a hot mantle plume stalls. In the brittle–plastic upper lithosphere, the magma flow is focused in dykes radiating from the focal region weakened by ascending melts and fluids. The dykes propagate at the level of neutral buoyancy in the crust and feed sills in the sedimentary basin.

region that forms at the brittle to plastic/viscous rheology transition, radiating dykes and sills within the sedimentary basin. A radial stress pattern is exerted by the deep mantle plume. The lithosphere is weakened by melts and fluids above the magmatic source region. The magma may ascend vertically in porous melt-rich channels in the viscous regime (Connolly & Podladchikov 2007; Keller *et al.* 2013) and spread laterally (away from the source region) at the level of neutral buoyancy. The magma transport in the brittle–plastic part of the lithosphere occurs in dykes. Most of the eruptions occur in the axial volcanic zone above the hot mantle plume. The level of neutral buoyancy deepens in the vicinity of the sedimentary basin as a result of the decrease in the density of the sediments relative to the adjacent basement rocks. The sills are fed by dykes (mostly from below) and spread sideways at weak sedimentary horizons. This conceptual picture forms the basis for our mechanical model that aims to infer the regional palaeo-stress field and associated geometry of dykes in the northern Barents Sea.

Mechanical models for dyke emplacement

Model geometry and problem setup

Mechanical modelling of the deformation associated with a magmatic reservoir is an important tool towards a better understanding of the emplacement process; see Grosfils *et al.* (2013) for elastic models and Gerbault (2012) for elastoplastic models. Specifically, the geometry of dykes in the horizontal plane is often explained using two-dimensional elastic mechanical models (Odé 1957; Muller & Pollard 1977; McKenzie *et al.* 1992; Hou *et al.* 2010). The setup of our mechanical model is inspired by these previous studies.

The model consists of an elastic (or elastoplastic) circular plate containing a circular hole and subject to a pressure and shear stress boundary conditions (Fig. 7a). The inner and outer radii are 200 and 1200 km, respectively. We use a plane strain approximation that is assumed to be valid at mid-crustal depths. The deformation related to the vertical stresses is ignored. Thus our model setup should be equivalent to an upper lithosphere weakened by a circular mantle plume. The effects of fluid/melt pressure, temperature and prescribed rules of strain softening are not included in our model. A more complete description of the problem would have to include a three-dimensional visco-elastoplastic thermomechanical model and multiphase physics. However, given the sparsity and uncertainty of the geological and geophysical data, we believe that our simplified model constitutes a reasonable first-order approach.

We further specify the inner boundary as a free surface that corresponds to a weak inner region. In our numerical experiments we explore the effect of far-field shear stress and the corresponding stress concentration around the central circular region weakened by the mantle plume. We start with isotropic boundary conditions, i.e. radial extension. We then proceed by introducing some amount of far-field pure shear.

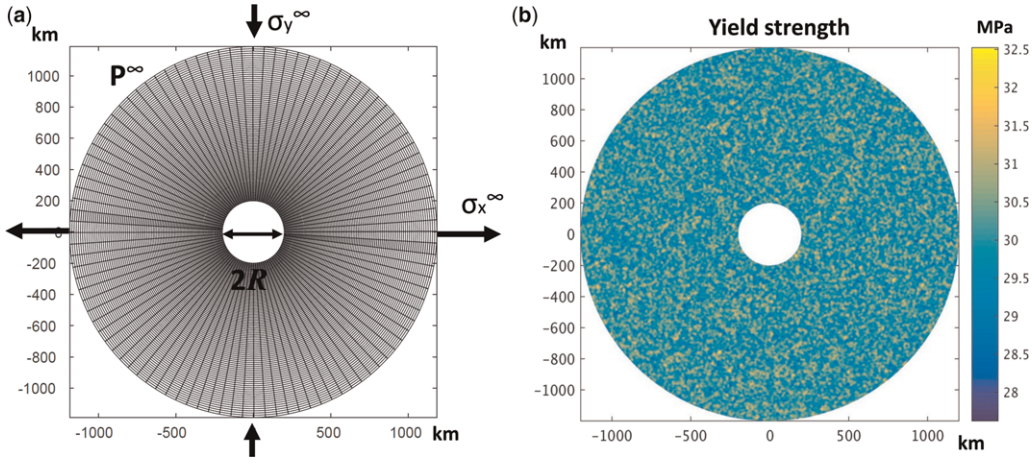

Fig. 7. General setup of analytical and numerical models. The model is in the horizontal plane. (**a**) Finite element mesh of the circular domain. The actual number of elements in the finite element model is 100 times larger than shown in the figure. The thick arrows show the boundary constraints applied along the perimeter of the model. R, radius of circular hole in the centre of the model (200 km); σ_x^∞, σ_y^∞, stresses at the outer radius; $p^\infty = (\sigma_x^\infty + \sigma_y^\infty)/2$, pressure at the outer boundary. (**b**) Random Gaussian field of the yield strength used in the setup of the numerical models. The correlation length is 8 km.

Analytical solution for elastic rheology

Let us first consider an analytical solution to the mechanical problem of stress concentration around a circular inclusion assuming that all the deformation is elastic. Yarushina & Podladchikov (2007) derived an analytical solution to a similar problem using the method of Muskhelishvili (1953). The model is subject to boundary conditions for homogeneous pressure ($\sigma_{rr} = p(t)$) and zero hoop stress ($\sigma_{r\theta} = 0$) at the inner boundary and the homogeneous horizontal stress components ($\sigma_{xx} = \sigma_{xx}^{\infty}(t)$, $\sigma_{yy} = \sigma_{yy}^{\infty}(t)$) and zero shear stress ($\sigma_{xy} = 0$) at the outer boundary. The solution for stresses is given by the following expressions:

$$\sigma_{rr} = p^{\infty} - \Delta P\left(\frac{R}{r}\right)^2 - \tau\left(1 - 4\left(\frac{R}{r}\right)^2 + 3\left(\frac{R}{r}\right)^4\right)\cos 2\theta \quad (1)$$

$$\sigma_{\theta\theta} = p^{\infty} + \Delta P\left(\frac{R}{r}\right)^2 + \tau\left(1 + 3\left(\frac{R}{r}\right)^4\right)\cos 2\theta \quad (2)$$

$$\sigma_{r\theta} = \tau\left(1 + 2\left(\frac{R}{r}\right)^2 - 3\left(\frac{R}{r}\right)^4\right)\sin 2\theta \quad (3)$$

where σ_{rr}, $\sigma_{\theta\theta}$, $\sigma_{r\theta}$ are the radial hoop and shear stress components, (r,θ) are polar coordinates, R is the inner radius, p^{∞} is the pressure at the outer boundary, ΔP is the pressure difference at the inner and outer radii and $\tau = (\sigma_{yy}^{\infty} - \sigma_{xx}^{\infty})/2$ is the shear stress at the outer boundary. Here and elsewhere in the paper, we assume that the tensile stresses are positive. The solution in terms of the maximum shear stress $\tau_{\max} = \sqrt{(\sigma_{yy} - \sigma_{xx})^2/4 + \sigma_{xy}^2}$ is presented for isotropic boundary conditions $\tau = 0$ (Fig. 8a) and for $\tau = \Delta P/2$ (Fig. 8b). The pressure gradient and far-field pressure (e.g. due to gravitational potential energy differences) is set to 10 MPa.

Geometry of tensile (mode I) fractures

The seismic velocity model in Figure 3 indicates no significant regional stretching of the crust. Therefore we suggest that the deformation associated with magma emplacement in the northern Barents Sea was localized by brittle–plastic failure of the crust linked to the process of dyking. According to Anderson's criterion, once the dyke is initiated it propagates normal to the least principal stress (Anderson 1937; Pollard 1973; Delaney *et al.* 1986). Odé (1957) used this idea to explain the radiating geometry of the Spanish Peaks dykes at the eastern edge of the Colorado Plateau. McKenzie *et al.* (1992) further developed this model to explain the geometry of dykes on Earth (the Mackenzie dyke swarm in the Canadian Shield) and Venus (associated with coronae structures) by constructing

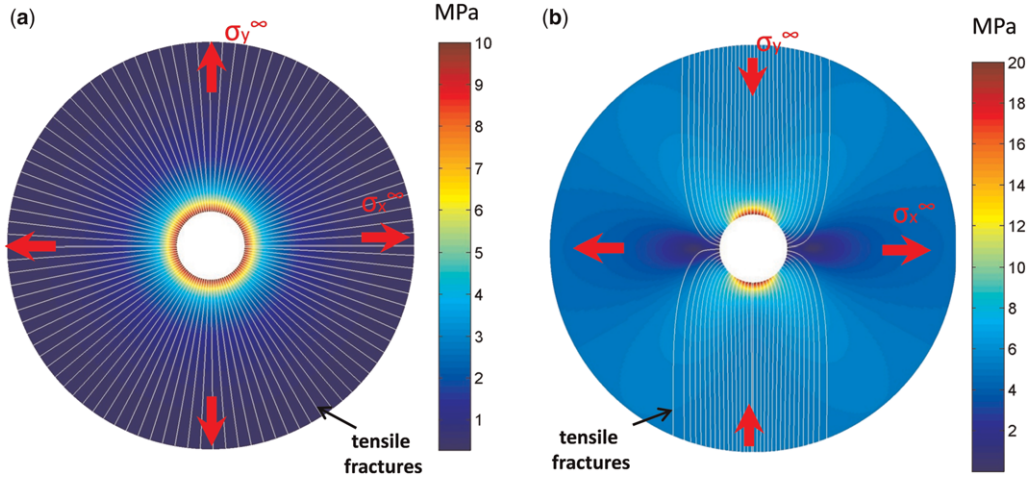

Fig. 8. Elastic analytical solutions for the maximum shear stress. Trajectories of the largest principal stress are shown in white for (**a**) pressure and (**b**) combined pressure and shear stress (pure shear) boundary conditions. These trajectories illustrate a possible geometry of tensile (mode I) fractures in the crust. Red arrows indicate direction of external loading. Note that the central area has higher stresses and therefore fractures will be initiated from the centre.

stress trajectories for the direction normal to the least compressive stress. These studies used an analytical solution for a perforated elastic plate in a plane strain approximation similar to that described previously. However, these researchers were mainly interested in the area far from the plume and made an assumption that $R/r \ll 1$, which implies that the radius of the circular hole is small compared with the distance from the centre of the hole. Alternatively, Hou *et al.* (2010) used a finite element model of a thin elastic plate with a large circular 'plug' stressed at the external boundaries to model the directions of the principal stresses, matching the geometry of dykes within the Mackenzie swarm.

Following these researchers, we derive the largest principal stress trajectories using the analytical elastic solution from equations (1)–(3) and solving numerically an ordinary differential equation:

$$\frac{\mathrm{d}y}{\mathrm{d}x} = \tan\theta(x, y), \tag{4}$$

in which the angle $\theta(x,y)$ determines the orientation of the principal stresses given that

$$\theta(x, y) = \frac{1}{2}\arctan\left(\frac{2\sigma_{xy}(x, y)}{\sigma_{xx}(x, y) - \sigma_{yy}(x, y)}\right). \tag{5}$$

We use a fourth-order Runge–Kutta method to integrate equations (4) and (5).

Without applied shear, the geometry of tensile fractures is radially symmetrical (Fig. 8a). Adding the far-field shear component leads to a deviation of the trajectories from a radial trend towards the direction nearly orthogonal to the extension (Fig. 8b). Deviation occurs at distances nearly equal to the plume diameter. Close to the plume, the tensile stress still exhibits a nearly radial pattern. These trajectories might represent the geometry of the dyke swarm if the initiating fractures were not interacting with each other, i.e. they were located at a considerable distance or were immediately healed after initiation by material with similar elastic properties.

To date, this model provides the most popular explanation of the geometry of dykes in giant swarms. The model is elegant, easy to implement and gives the required physical intuition based on the parameter $\tau/\Delta P$. This dependence can be slightly modified by the external pressure p^{∞}. The approach based on an elastic model may give the correct results for the case of a single fracture. However, each new fracture must modify the stress state and therefore the next dyke should be modelled using a slightly different stress distribution.

The geometry of dyke swarms suggests more complicated settings than those predicted by the elastic model. The density of dyke populations across the stress trajectories is not uniform. There are some preferred emplacement directions. The curvature of dykes can be different from the predictions. Dykes may swing and intersect each other.

The geophysical and geological observations provided in Figures 1 and 2 suggest that dykes which apparently belong to the same LIP event can intersect and can be affected by each other and local crustal heterogeneities. We interpret some magnetic anomalies (Fig. 2) as fractures (or shear zones) oriented orthogonal to the main strike of the dyke planes. The existence of shear zones cutting dykes is documented on Franz Josef Land (Dibner 1998). Geological observations on many islands of the archipelago indicate that some mafic intrusions cut the lava flows and the Early Cretaceous sedimentary rocks (Dibner *et al.* 1992). These observations suggest that the dykes within the swarm intruded neither independently nor simultaneously. We believe that a more consistent formulation for the modelling of fracture networks such as dyke swarms should include irreversible plastic deformation. However, analytical solutions for this type of problem are complicated and exist only for small values of $\tau/\Delta P$. Thus numerical solutions are required.

Numerical elastoplastic Model 1

The development of plastic deformation in the crust can be viewed either as the formation and growth of microcracks or sliding on grain boundaries. The upper crust is considered to deform through cataclastic faulting, whereas a semi-brittle regime is more typical at higher pressures (Hirth & Tullis 1994). This behaviour is well described using the Mohr–Coulomb yield criterion (F)

$$F = \tau_{\max} + \left(\frac{\sigma_{xx} + \sigma_{yy}}{2}\right)\sin\varphi - Y_{\mathrm{s}}, \tag{6}$$

where φ is the friction angle, Y_{s} is the yield stress and $\tau_{\max}$ is the maximum shear stress. In the elastoplastic models, the total strain rate can be decomposed on the elastic and plastic components as soon as the yield criterion $F = 0$ is reached (Yu 2007). Elastic components are still governed by Hooke's law, while plastic flow law is applied to the plastic components. This leads to additional dependence of the elastoplastic stiffness tensor on the stresses. The relationship between the strain rate and stress rate can be written as

$$\underline{\dot{\boldsymbol{\sigma}}} = \underline{\underline{\mathbf{D}}}^{\mathrm{ep}} \cdot \underline{\dot{\mathbf{e}}}^{\mathrm{total}}, \tag{7}$$

where $\underline{\dot{\mathbf{e}}}^{\mathrm{total}}$ is the total strain rate (written as a 3×1 vector for finite element numerical implementation), $\underline{\dot{\boldsymbol{\sigma}}}$ is the stress rate (3×1 vector) and $\underline{\underline{\mathbf{D}}}^{\mathrm{ep}}$ is a 3×3 elastoplastic tangent modular matrix that

depends on elastic and plastic material parameters and stresses, namely:

$$\underline{\underline{\mathbf{D}}}^{\mathrm{ep}} = \underline{\underline{\mathbf{D}}}\left(\frac{I - (\partial Q/\partial \underline{\boldsymbol{\sigma}})(\partial F/\partial \underline{\boldsymbol{\sigma}})\underline{\underline{\mathbf{D}}}}{(\partial F/\partial \underline{\boldsymbol{\sigma}})\underline{\underline{\mathbf{D}}}(\partial Q/\partial \underline{\boldsymbol{\sigma}})}\right) \quad (8)$$

D is the elastic stiffness matrix in plane strain; I is the identity matrix; Q is the plastic flow potential; σ is the stress (written as a vector).

Implicit in this equation is that plastic deformation is governed by the flow potential Q, which is usually taken in the form similar to the yield function

$$Q = \tau_{\max} + \left(\frac{\sigma_{xx} + \sigma_{yy}}{2}\right)\sin\psi + \text{const.} \quad (9)$$

Here ψ is the dilation angle that controls the volume increase during shear. We first consider the case of associated plastic flow. In the associative plasticity, the friction angle (φ) is equal to the dilatation angle ($\psi = \varphi$), which means that shear on the fault plane is accompanied by a similar component of volume increase.

Our numerical elastoplastic model is based on the formulation and the MATLAB code by Yarushina *et al.* (2010). The stresses are integrated using the finite element method (Zienkiewicz & Taylor 2005). We use a forward Euler incremental method for solving elastoplastic problems. The loading is incrementally increased towards the yield stress. The algorithm accounts for the drift from the yield surface and force equilibrium. The accuracy of the numerical solution is benchmarked v. elastic and elastoplastic analytical solutions by Yarushina *et al.* (2010).

The numerical grid consists of 1000 × 1000 elements with an adaptive cell size of 0.6 × 1.2 km close to the circular hole and 1.4 × 7.5 km at the outer boundary (Fig. 7a). We choose four-node isoparametric quadrilateral elements. The dimensions of the model are the same as in the elastic case (inner and outer radii 200 and 1200 km, respectively). The boundary conditions are pressure and the pure shear stress applied at the outer boundary. Both the friction and dilation angles are set to 30°. The yield stress in equation (6) is 30 MPa. The elastic parameters are a Poisson's ratio of 0.3 and a shear modulus of 30 GPa. Note that the elastic solution for stresses given in equations (1)–(3) is independent of the material parameters. The initial pressure at the outer boundary is 10 MPa. The values of the yield function (equation 6) are shown for isotropic stress (radial extension) boundary conditions (Fig. 9a) and combined pressure–shear loading at $\tau = \Delta P/2$ (Fig. 9b).

Geometry of shear (mode II) fractures

A number of previous studies suggested that the zones of shear failure may serve as pathways for magma migration in the crust (Regenauer-Lieb 1998; Weinberg & Regenauer-Lieb 2010; Gerbault 2012). In these models, the direction of shear failure and faulting in the crust is predicted using a plane strain slip-line theory. This approach has also been applied in other geodynamic settings (Tapponnier & Molnar 1976; Regenauer-Lieb & Petit 1997). The two sets of conjugate shear trajectories (α and

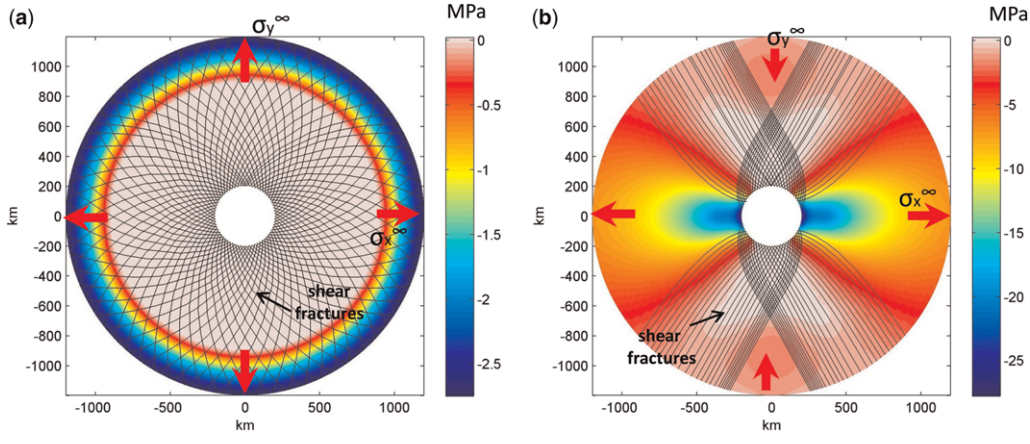

Fig. 9. Results of elastoplastic finite element Model 1 (associated plasticity). Mohr–Coulomb yield stress F (see equation 6) for (**a**) isotropic extension (pressure) boundary conditions and (**b**) combined pressure and shear stress (pure shear) boundary conditions: $\tau = -\Delta P/2$. Slip-lines illustrate a possible geometry of shear (mode II) fractures in the crust inside the plastic zone ($F = 0$)

β slip-lines) are found from an equation similar to equation (4):

$$\frac{dy}{dx} = \tan\left(\theta(x, y) \pm \left(\frac{\pi}{4} - \frac{\varphi}{2}\right)\right) \qquad (10)$$

The slip-lines represent the shear failure (mode II fracture) pattern inside the plastic zone (Fig. 9). For a purely isotropic load ($\sigma^{\infty}_{xx} = \sigma^{\infty}_{yy}$), the slip trajectories show a symmetrical fan-shaped logarithmic spiral pattern (Fig. 9a). A similar pattern of crustal fractures was previously obtained by Gerya (2014) using a three-dimensional numerical thermomechanical model of Venusian coronae structures. Applying a shear load ($\sigma^{\infty}_{xx} \neq \sigma^{\infty}_{yy}$) results in the formation of two pairs of conjugate fault populations bisected by the largest compressive stress (vertical) direction (Fig. 9b). The curvature of the slip-lines depends on the friction angle. However, it does not significantly affect the general pattern. It should be noted that the way the trajectories are computed using equation (9) does not depend on the specific problem and this technique can be used in models with different geometry and boundary conditions.

Using the slip-line approach we can predict the arcuate geometry of dilatant faults (Fig. 9). The geometry of slip-lines shows preferred directions (not axisymmetrical) when far-field shear is applied (Fig. 9b). The drawback of this approach is that the location and spacing of slip-lines is predefined by the numerical grid and not by rock heterogeneity or any other physical factor. Moreover, the experiments on rock deformation show that the dilation angle should decrease with the increase in strain and must be smaller than the friction angle ($\psi < \phi$). This leads to different kinematic and stress characteristics, implying that stress and strain will have localization along different directions. Laboratory experiments and field observations of borehole break-outs show that the localization of strain and stress occurs within shear bands that may deviate from slip-lines (Vardoulakis *et al.* 1988; Papamichos *et al.* 2010).

Numerical elastoplastic Model 2 and shear bands

The numerical Model 2 is similar to Model 1 except that we use a non-associative plastic flow law ($\psi < \phi$). Thus in this approach the yield function (F) is different from the flow potential (Q) ($F \neq Q$). This type of rheology leads to instabilities of deformation and the formation of shear bands (Rudnicki & Rice 1975). These are observed experimentally and have been modelled numerically (Cundall 1989). Dilational effects are very common in rocks during shear. This phenomenon is partly due to small asperities at the fault planes that dilate the fracture until the strain reaches some critical value (Vermeer & de Borst 1984). The critical yield stress can be higher in dilatant rocks because part of the elastic energy can be spent on the volume change before the material breaks in shear. However, laboratory and *in situ* observations of rock deformation show that the dilation angle is much smaller than the friction angle and is typically around $\psi = 8^{\circ}$, whereas the friction angle is typically around $\phi = 30^{\circ}$ (Vermeer & de Borst 1984). The boundary conditions are the same as in Model 1 (Fig. 7). The development of plastic shear bands around a magma chamber was previously studied using numerical elastoplastic modelling by Gerbault (2012). The model proposed in this study can be viewed as a larger scale implementation of the approach presented by Gerbault (2012).

Our numerical experiments show that initial (physical) heterogeneity is required for localization by shear banding. Tests with homogeneous models and without applied shear did not show localization of deformation in shear bands. Small-scale heterogeneities are intrinsic to the crust, as indicated by seismological studies of the coda (scattered) waves associated with regional seismic phases (Sato *et al.* 2012). Thus we impose an initial random isotropic field on the yield stress (Fig. 7b). We use a Gaussian autocorrelation function to make a random realization. The maximum amplitude of heterogeneity is 8% and the correlation length is *c.* 8 km.

The regime of isotropic extension (pressure boundary condition) results in a fan-shaped logarithmic spiral pattern of dilatant shear bands (Figs 10a & 11a). The shear bands initiate at the inner boundary adjacent to the assumed mantle plume and propagate outwards while the far-field pressure is incrementally increased (Figs 10 and 11). The angle of the shear bands with respect to the largest principal stress lies in the range of the Coulomb ($\pi/4 - \varphi/2$) to the Arthur angle ($\pi/4 - (\varphi + \psi)/4$) (Vermeer & de Borst 1984). Both the pressure (Fig. 10) and shear stress (Fig. 11) are reduced within the shear bands. Thus the material softening in our model is not prescribed, but results from the formation of shear bands. The observed dilatation and weakening is favourable for the focusing of fluid or magma inside the deformation bands because much lower fluid (magma) pressures are needed to overcome resistance from the rock. The shear bands turn beyond one diameter to the shear direction following the Coulomb angle when shear loading is applied (Figs 10b & 11b). The geometry of shear bands is bisected by the direction of the far-field largest compressive stress. The strain localization in our mechanical model is caused by the rheological instability and does not involve any prescribed weakening rule.

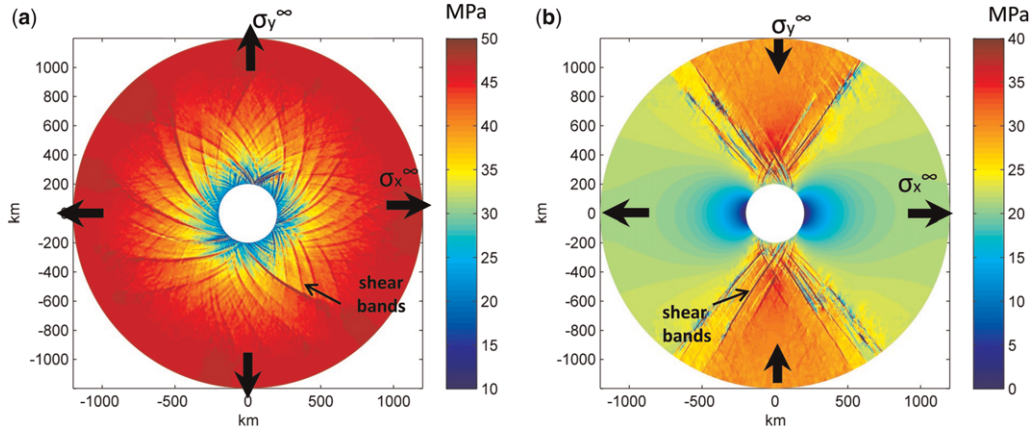

Fig. 10. Results of elastoplastic finite element Model 2 (non-associated plasticity). The pressure field is shown for (**a**) isotropic extension (pressure) boundary conditions and (**b**) combined pressure and shear stress (pure shear) boundary conditions: $\tau = -\Delta P/2$. Thick arrows show the boundary constraints applied along the perimeter of the model. The extension pressure is positive. Note that most shear bands are under-pressured (i.e. dilating).

Our results show that the mechanical model, including the non-associated elastoplastic rheology, is a suitable approach to describe the deformation around the plume centre. It captures the general pattern of the two conjugate dyke swarms in the northern Barents Sea (Figs 1 & 2). The dilatant shear bands initiate on random (physical, not numerical) small-scale heterogeneities in the crust and propagate away from the magmatic centre. We propose that under-pressured weak shear bands facilitate magma transport in the vicinity of the source region. The propagation of fractures further away from the magmatic centre is further addressed in the following sections. For instance, the dykes may change the propagation regime from mode II to mode I fracture depending on the local state of stress.

Discussion

Palaeo-reconstruction of Amerasia Basin and geometry of dyke swarms

Pre-break-up reconstructions of the Amerasia Basins often juxtapose the East Siberian and Arctic Alaska margin with the Canadian Arctic margin in

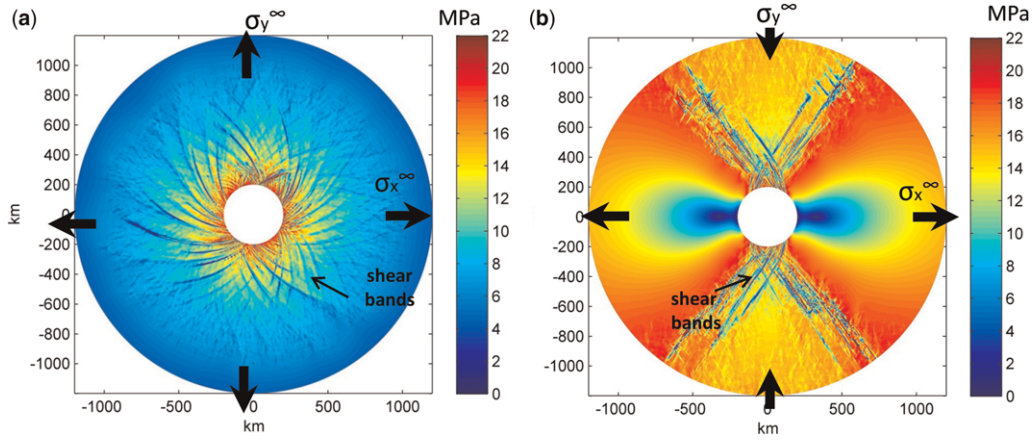

Fig. 11. Results of elastoplastic finite element Model 2 (non-associated plasticity). The maximum shear stress field is shown for (**a**) isotropic extension (pressure) boundary conditions and (**b**) combined pressure and shear stress (pure shear) boundary conditions: $\tau = -\Delta P/2$. Thick arrows show the boundary constraints applied along the perimeter of the model. Note low shear stress inside shear bands.

the Early Cretaceous epoch (Sweeney 1985; Grantz *et al.* 1998; Lawver *et al.* 2002; Drachev & Saunders 2006; Drachev 2011; Shephard *et al.* 2013). These kinematic models imply a counter-clockwise rotation of the Arctic Alaska plate at the spreading axis oriented nearly orthogonal to the northern Barents Sea margin. In this study, we use a similar pre-break-up kinematic reconstruction of the Amerasia Basin (Fig. 12a) that generally follows the model of Shephard *et al.* (2013). In addition, it includes the Chukchi Borderland and Bennett Island located north of Franz Josef Land (Drachev & Saunders 2006). It should be noted that the relative position of the New Siberian Islands is not accurately restored in Figure 12 due to Late Cretaceous–Cenozoic extension in the East Siberian Shelf (Drachev *et al.* 2010; Drachev 2011). The positions of Ellesmere and Axel Heiberg islands are modified as a result of Early Cenozoic compression and the formation of the Eurekan fold–thrust belt (Piepjohn *et al.* 2007). In Figure 12a, Ellesmere and Axel Heiberg islands are shifted towards Greenland relative to the model of Shephard *et al.* (2013). The light grey lines for Arctic Canada indicate the location of coastlines in the reconstruction by Shephard *et al.* (2013).

This configuration creates geometrical problems fitting in the Lomonosov Ridge when the Eurasia Basin is closed. The previously published configuration of Ellesmere Island has been tentatively introduced to account for the Eurekan compression by fixing the northern coastline and extending Ellesmere and Axel Heiberg islands to the south. However, the amount of compression and the exact location of the blocks that composed the Ellesmere and Axel Heiberg islands are poorly constrained (G. Shephard pers. comm. 2016). In the presented reconstructions, we have moved the entire block by *c.* 200 km to the south. This configuration provides a more reasonable configuration with respect to the closure of the Eurasia Basin.

Four areas of Early Cretaceous magmatism can be identified in the circum-Arctic region: East Svalbard, Franz Josef Land, Arctic Canada and the area adjacent to the Arctic Alaska margin and Bennett Island (Drachev & Saunders 2006; Tegner & Pease 2014). The geometry of dykes in the northern Barents Sea is proposed in Figs 1 & 2. The geometry of dykes in Arctic Canada (Fig. 12a) follows Buchan & Ernst (2006). The Canadian dykes strike obliquely (30–45°) with respect to the passive margin. The quadruple spatial distribution of magmatism

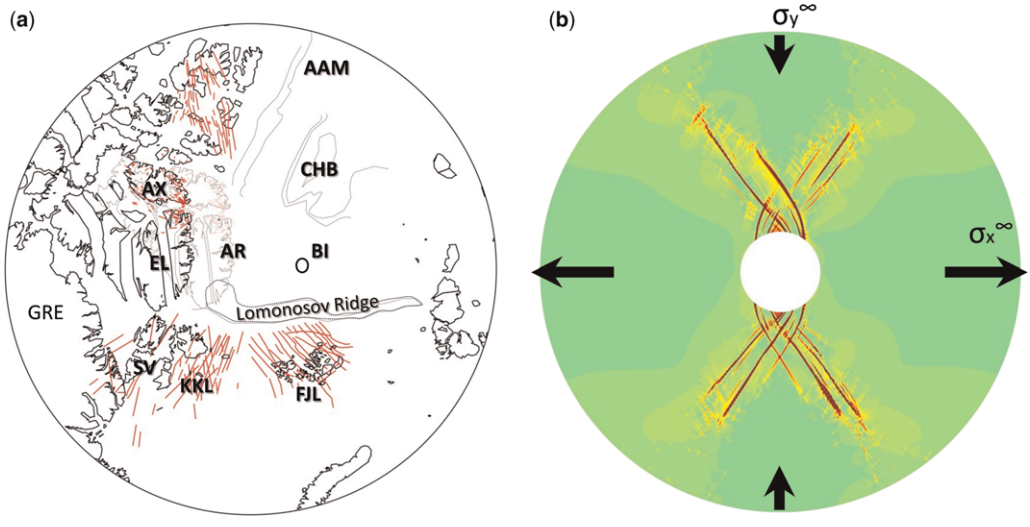

Fig. 12. Geometry of the High Arctic large igneous province dyke swarms. (**a**) Mafic dykes on top of the plate kinematic reconstruction for the Arctic region at *c.* 140 Ma. The kinematic model follows Shephard *et al.* (2013). In this study, Ellesmere and Axel Heiberg islands are moved towards Greenland by *c.* 200 km to account for the early Cenozoic Eurekan orogeny. The configuration of Ellesmere and Axel Heiberg islands in the model by Shephard *et al.* (2013) is shown using thinner lines. (**b**) The maximum (plastic) shear strain computed for combined pressure and pure shear stress boundary conditions ($\tau = -\Delta P/2$). The plastic strain is localized within shear bands. Geometry of dykes in Arctic Canada follows Buchan & Ernst (2006). AAM, Artic Alaska margin; AR, Alpha Ridge and tentative location of magmatic centre; AX, Axel Heiberg Island; BI, Bennett Island; CHB, Chukchi Borderland; EL, Ellesmere Island; FJL, Franz Josef Land; GRE, Greenland; KKL, Kong Karls Land; SV, Svalbard. Thin grey lines show isobath −1600 m at the Arctic Alaska Margin and Chukchi Borderland.

forms a pattern that resembles the conjugate families of dilatant plastic shear bands obtained in our numerical experiments when a far-field shear stress was applied at the outer boundary (Figs 10b, 11b & 12b). However, taking into account the complexities of the local stress state and the younger deformation, we do not attempt to match the exact geometry of dykes in the circum-Arctic region.

At the same time, we find that the general pattern of dykes in the northern Barents Sea (Fig. 12a) is well captured by the geometry of dilatant shear bands in our model (Fig. 12b). This can be interpreted in terms of dyke emplacement controlled by conjugate shear directions away from a magmatic centre north of the northern Barents Sea margin. We suggest that the network of dilatant shear bands served as pathways for magma and/or developed concurrent to magma emplacement (see also discussion on the problem of magma transport in the next section). Similarly, our model can explain the orientation of dykes in the Sverdrup Basin of Arctic Canada, including Axel Heiberg Island and Ellesmere Island (Fig. 12a). However, the initial geometry of dykes in this region could be modified by younger deformation.

Based on existing laboratory experiments (Holtzman *et al.* 2003; Katz *et al.* 2006) and numerical models (Keller *et al.* 2013; Gerya *et al.* 2015; Gerya & Burov 2015), we anticipate that the magmatic weakening of the lithosphere, associated with the axial volcanic zone and magma-rich shear bands, should have evolved rapidly (within 1–2 myr) through continental break-up to the development of an oceanic spreading centre where most of the volcanic activity should occur. However, this model is complicated by observations of a younger Cretaceous volcanism on the Arctic Canada margin.

Recent U–Pb dating results for the timing of magmatism in the Arctic Canada islands were reported by Evenchick *et al.* (2015). These researchers analysed samples from the Cretaceous dolerite sills and volcaniclastic rocks on Ellef Ringnes Island. The U–Pb dating of intrusive rocks gave ages of 126–120 Ma, similar to Corfu *et al.* (2013). The volcaniclastic rocks are younger (*c.* 105–101 Ma). This probably indicates prolonged volcanic activity after the main intrusive event at 126–120 Ma. The volcanic activity could be associated with a seafloor spreading centre parallel to the Arctic Canada margin and the formation of the Alpha Ridge volcanic plateau (e.g. Funck *et al.* 2011). The prolonged volcanism on the Arctic Canada margin is also indicated by the radioisotopic and geochemical analyses of silicic volcanic rocks on the northern coast of Ellesmere Island (*c.* 104–97 Ma) (Estrada *et al.* 2016). We can speculate that lithosphere rifting in combination with small-scale mantle convection (e.g. the model of Nielsen & Hopper 2004) could be responsible for this younger (post-break-up) volcanic activity on the rifted margin of Arctic Canada. By contrast, the Barents Sea margin was probably located farther away from the plume centre and was separated by the Lomonosov Ridge microcontinent. This can explain the lack of younger Cretaceous volcanism on the Barents Sea margin.

The pre-break-up reconstruction of Greenland suggests that some dykes in northern Greenland could belong to the Svalbard swarm. However, recent U–Pb dating of several dykes in this region has shown much younger ages of *c.* 85–80 Ma (Thórarinsson *et al.* 2015). Early Cretaceous basalts are also found in the Chukchi Borderland and Bennett Island (Drachev & Saunders 2006), but the resolution of magnetic data in this region is not high enough to identify dykes.

We propose that the High Arctic LIP dykes were initiated by utilizing a fracture pattern originating from a plume-related pressure gradient and regional far-field shear stress in the continental lithosphere. The geometry of dykes in large swarms is shown to be controlled by regional principal stresses. Pre-existing heterogeneities in the crust can lead to local stress concentrations, which might only locally alter the dyke geometry and not affect the regional pattern. A combination of extension related to the opening of the Canada Basin and a smaller compressional component during the Early Cretaceous can explain the mode of lithospheric failure and the emplacement of mafic dyke swarms in the Arctic region (Fig. 12b). The direction of the largest tensile stress follows the kinematic model for the opening of the Canada Basin sub-parallel to the northern Barents Sea margin. On the palaeo-Pacific side, some compression can be related to multiple terrain accretion along the Koyukuk–Nutesyn and Farallon subduction zones (Shephard *et al.* 2013).

Timing of break-up

The magmatic weakening of the proto-Arctic lithosphere associated with the LIP would subsequently lead to continental break-up and the initiation of seafloor spreading in the Amerasia Basin shortly after 124–122 Ma. The assumption of earlier seafloor spreading in the Amerasia Basin, as suggested by Grantz *et al.* (2011) and other publications, would create a mechanical problem: the deformation must have been focused in the weakest region (i.e. at the mid-ocean ridge or plate boundary) and failure of adjacent thick continental crust and concurrent dyke emplacement would not have occurred.

Døssing *et al.* (2013), based on the interpretation of new aeromagnetic data, have suggested that the Franz Josef Land and Arctic Canada dyke swarms might also cross the Alpha Ridge and adjacent Lomonosov Ridge margin. The formation of the

Alpha Ridge would definitely post-date the time of break-up. The seismic velocity structure of the Alpha Ridge indicates that the crustal thickness of this structure is *c.* 30 km (Funck *et al.* 2011). About two-thirds of the crust has P-wave velocities >7.1 km s^{-1}, suggesting a mafic igneous crystalline basement. Dredging and seismic reflection data indicate thick basaltic cover at shallower levels. We assume that even if some fragments of continental crust intruded by dykes were preserved below the basalts, these fragments must have been highly attenuated and deformed. In our opinion, the linear magnetic anomalies on the Alpha Ridge, mapped by Døssing *et al.* (2013), are more likely to be related to structures of oceanic rifting with excess magmatism (similar to the Icelandic rift zones). The discrepancy of a large amount of extension in the Amerasia Basin and very little regional extension in the northern Barents Sea would require a mechanical decoupling of these two regions at post-break-up times.

Another argument constraining the timing of continental break-up is the requirement of an area of continental denudation north of the Barents Sea margin during Barremian–Aptian time. This is suggested by Barremian–Aptian fluvial deposits in the Barents Sea and Svalbard linked to tectonic uplift in the north (Maher 2001; Midtkandal & Nystuen 2009). The river deltas were prograding into southerly regions during Barremian time (Smelror *et al.* 2009). The MCS data in the central Barents Sea show clinoforms prograding from the north and NE source areas to the southern sink region (Dimitriou 2014; Midtkandal *et al.* 2015). The transition from mainly shale to the Barremian sandstone units is responsible for a regional stratigraphic horizon throughout the northern Barents Sea (Grogan *et al.* 1999). On Svalbard, the Helvetiafjellet Formation is associated with a change of palaeoenvironment from marine to nearshore–continental containing coal layers and footprints of dinosaurs. The Isachsen Formation in the Sverdrup Basin of Arctic Canada and the Kuparuk Formation in north Alaska (Leith *et al.* 1992) can be considered as analogues to the Helvetiafjellet Formation and linked to the plume-related surface topography.

Magma transport within East Barents Sea Basin

Understanding the mechanism of magmatic intrusions into sedimentary basins has important implications for the petroleum industry and palaeoclimatic research. Seismic data and borehole information obtained within the East Barents Sea Basin indicate the presence of a dolerite sill complex that seemingly extends throughout the entire basin (Shipilov & Karyakin 2011; Polteau *et al.* 2016; and this paper). At the same time, the eastern branch of the dyke swarm south of Franz Josef Land cuts the northern East Barents Basin nearly orthogonally (some dykes swing slightly towards the basin in the western part of the archipelago; Figs 1 & 2). Possible mechanisms controlling the transport of magma in the continental crust away from the plume-related magmatic source region into the Barents Sea are discussed in the following paragraphs.

The zone of shear failure has been suggested to facilitate magmatic transport away from an upper crustal magma chamber (Gerbault 2012) in the form of anastomosing dykes at deep crustal levels (Weinberg & Regenauer-Lieb 2010) and on lithospheric scales associated with Alpine collision (Regenauer-Lieb 1998). Localized melt bands oriented along the shear directions have been observed in laboratory experiments of the deformation of partially molten aggregates (Holtzman *et al.* 2003; Katz *et al.* 2006). White *et al.* (2011) reported mainly double-couple earthquake mechanisms (mode II fracture) associated with dyke propagation from mid-crustal depths in Iceland. Laboratory experiments on quartz aggregates by Hirth & Tullis (1994) indicate a transition from dominant mode I to dominant mode II microfracturing at about 0.6 GPa. In nature, the depth of this transition is probably also controlled by temperature and composition. Thus the dilatant plastic shear bands may facilitate the migration of magma where the mode I fractures are inhibited by higher confining pressure, temperature and other reasons.

The lateral propagation of magma in dykes is assumed to be driven by magma pressure at the source region and topographic gradients (Fialko & Rubin 1999). Theoretical models (e.g. Lister & Kerr 1991) predict the lateral propagation of dykes in the crust along the level of neutral buoyancy. The effect of the topographic gradient (or, more generally, the gravitational potential energy difference) on the dyke propagation path has been illustrated by monitoring the growth of a 45 km long dyke in Iceland (Sigmundsson *et al.* 2015). Both theory and observations suggest that a laterally spreading dyke can propagate into an area with falling lithostatic pressure and that the depth of propagation is controlled by the level of neutral buoyancy. The lithostatic pressure at a given depth and the depth to the level of neutral buoyancy must have been deeper in the sedimentary basin than in Franz Josef Land. Thus this may partly explain the reorientation of magma flow towards the East Barents Sea Basin.

The extent of a vertical v. horizontal magma transport mechanism in the lithosphere cannot be ruled out. The study of anisotropic magnetic susceptibility of the Mackenzie dyke swarm by Ernst & Baragar (1992) suggests that the flow within the

dykes is mostly vertical within a *c.* 500 km horizontal distance from the magmatic centre and is mostly horizontal farther away. Taking this as a first-order estimate, the transport of magma within the East Barents Sea Basin might have occurred through lateral flow at the level of neutral buoyancy.

The surface topography, as another controlling parameter at the time of emplacement, can be inferred based on structural and lithological constraints. Grogan *et al.* (2000) interpreted north–NW-trending flexures at the Mesozoic level within the Kong Karls Land platform in multichannel seismic data. The flexure developed above the Late Palaeozoic faults reactivated in the Late Mesozoic and Cenozoic. The field relations indicate that flood basalts in Kong Karls Land were extruded on top of a nearly flat landscape. Following their arguments, the flexure was filled in by the lowermost fluvial sediments of the Helvetiafjellet Formation before the eruption. These observations indicate that the elevated topography north of the Barents Sea margin initiated before the eruption of flood basalts in Kong Karls Land.

Another prominent topographic feature in the Barents Sea region is the NNE–SSW-oriented Novaya Zemlya fold belt. This fold belt follows the eastern flank of the East Barents Basin and was probably formed in the Triassic to earliest Jurassic (Drachev *et al.* 2010). Palaeogeographical reconstructions for the Cretaceous period indicate that Novaya Zemlya was a highland region (Smelror *et al.* 2009). Thus this elevated topography could affect the stress regime and propagation path of dykes. The faults and zones of weakness associated with this fold belt could also provide zones of increased permeability. In addition, the distribution of gravitational potential energy in the Barents Sea could lead to the rotation of principal stresses from horizontal to vertical planes. This would change the preferred mode of magma emplacement from dykes to sills. The poro-elastoplastic numerical models of Rozhko *et al.* (2007) suggest that fluid-filled fractures pressurized from below tend to develop as vertical dykes or V-shaped intrusions in horizontal extension, whereas sub-horizontal intrusions develop in a compressive stress regime. Thus the compression associated with surface topography changes could contribute to the formation of the thick sill complex in the East Barents Sea Basin. A geological analogue to the East Barents Sea intrusive complex is the dolerite intrusions along the deformation front of the Transantarctic Mountains associated with the Ferrar LIP (Elliot *et al.* 1999). Ernst *et al.* (1995) provided other geological examples of sedimentary basins intruded by sills fed by dyke swarms.

Porous flow localized by a channelling instability (Connolly & Podladchikov 2007; Yarushina *et al.* 2015) is another mechanism of magma transport as an alternative to fluid-filled fractures. Such fluid flow initiates in response to fluid overpressure and propagates in the direction of the pressure gradients. The formation of dyke-like features by the mechanism of shear fractures explained in this paper may be accompanied by such processes. This model could probably explain the kilometre-scale thickness of vertical column-like anomalies observed in the seismic reflection images and tomographic velocity models (Figs 3 & 5). The next step towards understanding the transport of magma in dykes and sills should be the implementation of two-phase visco-elastoplastic deformation models such as those presented by Keller *et al.* (2013) and Yarushina *et al.* (2015). The effect of the three-dimensional stress field should also be taken into account.

Conclusions

Geophysical and geological data in the Barents Sea indicate that an area in excess of 1.5×10^6 km^2 has been affected by Early Cretaceous volcanism. The northern Barents Sea was affected by two dolerite dyke swarms in the eastern Svalbard and Franz Josef Land regions. Multichannel seismic data indicate that the dykes fed the dolerite sills and resided in Permian to Early Cretaceous sedimentary strata in the northern Barents Sea. The dyke-like anomalies penetrate the entire sedimentary cover in the multichannel seismic data. Wide-angle seismic data indicate that the dykes or feeder channels may extend to mid-crustal depths (15–20 km) and possibly deeper. The Moho depth below the igneous province of 30–37 km is evidence that significant lithosphere thinning and decompressional melting did not occur. Seismic velocities in the lower crust do not exceed 7.1 km s^{-1}, indicating a lack of underplating. We infer a localized mode for both deformation and magmatic transport within the crust.

These observations can be explained by magma transport in dykes radiating from a hotspot region north of the Barents Sea margin shortly before the Amerasia Basin continental break-up. In support of this idea, we considered a two-dimensional plane strain elastoplastic finite element model. The geometry of dykes in the northern Barents Sea region is predicted by the pattern of dilatant plastic shear bands in a model containing a circular hole with a radius of 200 km and subject to combined far-field extension pressure and pure shear load. Dilatant plastic shear bands are suggested to control magmatic transport in the northern Barents Sea. Other mechanical models for the formation of dyke swarms were discussed and their strengths and shortcomings highlighted. We suggest that the

far-field shear stress in the Early Cretaceous resulted from a combination of extension in the Amerasia Basin sub-parallel to the northern Barents Sea margin and orthogonal compression related to palaeo-Pacific subduction.

A. Minakov and J. I. Faleide acknowledges support from VISTA, project number 6264, and the Research Council of Norway through its Centres of Excellence funding scheme, project number 223272. We also thank Anna Mironova for helping to produce Figure 6.

References

Abashev, V., Mikhaltsov, N. & Vernikovsky, V. 2015. Paleomagnetism of Jurassic–Cretaceous basalts from the Franz Josef Land Archipelago: tectonic implications. Geophysical Research Abstracts Vol. **17**, EGU2015-797, 2015 EGU General Assembly 2015, 12–17 April, 2015, Vienna, Austria, http://meetingorganizer.copernicus.org/EGU2015/EGU2015-797.pdf

Anderson, E.M. 1937. IX. The dynamics of the formation of cone-sheets, ring-dykes, and caldron-subsidences. *Proceedings of the Royal Society of Edinburgh*, **56**, 128–157.

Bailey, J.C. & Rasmussen, M.H. 1997. Petrochemistry of Jurassic and Cretaceous tholeiites from Kong Karls Land, Svalbard, and their relation to Mesozoic magmatism in the Arctic. *Polar Research*, **16**, 37–62.

Becker, J.J., Sandwell, D.T. *et al.* 2009. Global bathymetry and elevation data at 30 arc seconds resolution: SRTM30_PLUS. *Marine Geodesy*, **32**, 355–371.

Breivik, A.J., Mjelde, R., Grogan, P., Shimamura, H., Murai, Y. & Nishimura, Y. 2005. Caledonide development offshore–onshore Svalbard based on ocean bottom seismometer, conventional seismic, and potential field data. *Tectonophysics*, **401**, 79–117.

Buchan, K.L. & Ernst, R. 2006. Giant dyke swarms and the reconstruction of the Canadian Arctic islands, Greenland, Svalbard and Franz Josef Land. *In*: Hanski, E., Mertanen, S., Rämö, T. & Vuollo, J. (eds) *Dyke Swarms – Time Markers of Crustal Evolution*. Taylor and Francis/Balkema, London, 27–48.

Buck, W.R. 2006. The role of magma in the development of the Afro-Arabian Rift System. *In*: Yirgu, G., Ebinger, C.J. & Maguire, P.K.H. (eds) *The Afar Volcanic Province within the East African Rift System*. Geological Society, London, Special Publications, **259**, 43–54.

Buiter, S.J. & Torsvik, T.H. 2014. A review of Wilson cycle plate margins: a role for mantle plumes in continental break-up along sutures? *Gondwana Research*, **26**, 627–653.

Coffin, M.F. & Eldholm, O. 1994. Large igneous provinces: crustal structure, dimensions, and external consequences. *Reviews of Geophysics*, **32**, 1–36.

Connolly, J.A.D. & Podladchikov, Y.Y. 2007. Decompaction weakening and channeling instability in ductile porous media: implications for asthenospheric melt segregation. *Journal of Geophysical Research: Solid Earth*, **112**, B10205, https://doi.org/10.1029/2005JB004213

Corfu, F., Polteau, S., Planke, S., Faleide, J.I., Svensen, H., Zayoncheck, A. & Stolbov, N. 2013. U–Pb geochronology of Cretaceous magmatism on Svalbard and Franz Josef Land, Barents Sea large igneous province. *Geological Magazine*, **150**, 1127–1135.

Cundall, P.A. 1989. Numerical experiments on localization in frictional materials. *Ingenieur-Archiv*, **59**, 148–159.

Delaney, P.T., Pollard, D.D., Ziony, J.I. & McKee, E.H. 1986. Field relations between dikes and joints: emplacement processes and paleostress analysis. *Journal of Geophysical Research: Solid Earth*, **91**, 4920–4938.

Dibner, V.D. 1998. *Geology of Franz Josef Land*. Norsk Polarinstitutt, Oslo.

Dibner, V., Bro, E., Pchelina, T., Preobrajenskaja, E. & Shkola, I. 1992. Geology of the Franz Josef Land archipelago, Russian Federation. Paper presented at the *International Conference on Arctic Margins (ICAM 1992)*, September 1992, Anchorage, AK, USA, 13, pp. 1–16, https://www.boem.gov/ICAM92-167/

Dimitriou, M. 2014. *Lower Cretaceous prograding units in the eastern part of the SW Barents Sea*. Master thesis, University of Oslo.

Drachev, S. & Saunders, A. 2006. The Early Cretaceous Arctic LIP: its geodynamic setting and implications for Canada Basin opening. Paper presented at the *Proceedings of the Fourth International Conference on Arctic Margins (ICAM IV)*, Dartmouth, Nova Scotia, Canada September 30–October 3, 2003. *In*: Scott, R.A. & Thurston, D.K. (eds) Published by U.S. Department of the Interior Anchorage, Minerals Management Service, Alaska Outer Continental Shelf Region, Alaska, October, 2006 https://www.diva-portal.org/smash/get/diva2:207900/FULLTEXT01.pdf

Drachev, S.S. 2011. Tectonic setting, structure and petroleum geology of the Siberian Arctic offshore sedimentary basins. *In*: Spencer, A.M., Embry, A.F., Gautier, D.L., Stoupakova, A.V. & Sørensen, K. (eds) *Arctic Petroleum Geology*. Geological Society, London, Memoirs, **35**, 369–394.

Drachev, S.S., Malyshev, N.A. & Nikishin, A.M. 2010. Tectonic history and petroleum geology of the Russian Arctic Shelves: an overview. *In*: Vining, B.A. & Pickering, S.C. (eds) *Petroleum Geology: From Mature Basins to New Frontiers – Proceedings of the 7th Petroleum Geology Conference*. Geological Society, London, 591–5619.

Døssing, A., Jackson, H.R., Matzka, J., Einarsson, I., Rasmussen, T.M., Olesen, A.V. & Brozena, J.M. 2013. On the origin of the Amerasia Basin and the High Arctic large igneous province – results of new aeromagnetic data. *Earth and Planetary Science Letters*, **363**, 219–230.

Ebinger, C.J. & Casey, M. 2001. Continental breakup in magmatic provinces: an Ethiopian example. *Geology*, **29**, 527–530.

Eldholm, O. & Grue, K. 1994. North Atlantic volcanic margins: dimensions and production rates. *Journal of Geophysical Research: Solid Earth*, **99**, 2955–2968.

Elliot, D.H., Fleming, T.H., Kyle, P.R. & Foland, K.A. 1999. Long-distance transport of magmas in the Jurassic Ferrar large igneous province, Antarctica. *Earth and Planetary Science Letters*, **167**, 89–104.

Ernst, R.E. 2014. *Large Igneous Provinces*. Cambridge University Press, Cambridge.

Ernst, R.E. & Baragar, W.R.A. 1992. Evidence from magnetic fabric for the flow pattern of magma in the Mackenzie giant radiating dyke swarm. *Nature*, **356**, 511–513.

Ernst, R.E., Head, J.W., Parfitt, E., Grosfils, E. & Wilson, L. 1995. Giant radiating dyke swarms on Earth and Venus. *Earth-Science Reviews*, **39**, 1–58.

Ernst, R.E., Bleeker, W., Söderlund, U. & Kerr, A.C. 2013. Large igneous provinces and supercontinents: toward completing the plate tectonic revolution. *Lithos*, **174**, 1–14.

Estrada, S., Damaske, D., Henjes-Kunst, F., Schreckenberger, B., Oakey, G.N., Piepjohn, K. & Linnemann, U. 2016. Multistage Cretaceous magmatism in the northern coastal region of Ellesmere Island and its relation to the formation of Alpha Ridge – evidence from aeromagnetic, geochemical and geochronological data. *Norwegian Journal of Geology*, **96**, 65–95.

Evenchick, C.A., Davis, W.J., Bédard, J.H., Hayward, N. & Friedman, R.M. 2015. Evidence for protracted High Arctic large igneous province magmatism in the central Sverdrup Basin from stratigraphy, geochronology, and paleodepths of saucer-shaped sills. *Geological Society of America Bulletin*, B31190.1, https://doi.org/10.1130/B31190.1

Faleide, J.I., Tsikalas, F. *et al*. 2008. Structure and evolution of the continental margin off Norway and the Barents Sea. *Episodes*, **31**, 82–91.

Farra, V. & Madariaga, R. 1987. Seismic waveform modeling in heterogeneous media by ray perturbation theory. *Journal of Geophysical Research*, **92**, 140–146.

Fialko, Y.A. & Rubin, A.M. 1999. Thermal and mechanical aspects of magma emplacement in giant dike swarms. *Journal of Geophysical Research: Solid Earth*, **104**, 23033–23049.

Funck, T., Jackson, H.R. & Shimeld, J. 2011. The crustal structure of the Alpha Ridge at the transition to the Canadian Polar Margin: results from a seismic refraction experiment. *Journal of Geophysical Research: Solid Earth*, **116**, B12101.

Gac, S., Huismans, R.S., Podladchikov, Y.Y. & Faleide, J.I. 2012. On the origin of the ultradeep East Barents Sea basin. *Journal of Geophysical Research: Solid Earth*, **117**, B04401.

Gaina, C., Werner, S.C., Saltus, R. & Maus, S. 2011. Circum-Arctic mapping project: new magnetic and gravity anomaly maps of the Arctic. *In*: Spencer, A.M., Embry, A.F., Gautier, D.L., Stoupakova, A.V. & Sørensen, K. (eds) *Arctic Petroleum Geology*. Geological Society, London, Memoirs, **35**, 39–48.

Gerbault, M. 2012. Pressure conditions for shear and tensile failure around a circular magma chamber; insight from elasto-plastic modelling. *In*: Healy, D., Butler, R.W.H., Shipton, Z.K. & Sibson, R.H. (eds) *Faulting, Fracturing and Igneous Intrusion in the Earth's Crust*. Geological Society, London, Special Publications, **367**, 111–130.

Gernigon, L. & Brönner, M. 2012. Late Palaeozoic architecture and evolution of the southwestern Barents Sea: insights from a new generation of aeromagnetic data. *Journal of the Geological Society, London*, **169**, 449–459.

Gerya, T. & Burov, E. 2015. Formation and stability of ridge-ridge-ridge triple junctions in rheologically realistic lithosphere model. Geophysical Research Abstracts, Vol. **17**, EGU2015-15090, 2015 EGU General Assembly, 12–17 April 2015, Vienna, Austria, http://meetingorganizer.copernicus.org/EGU2015/EGU2015-15090.pdf

Gerya, T.V. 2014. Plume-induced crustal convection: 3D thermomechanical model and implications for the origin of novae and coronae on Venus. *Earth and Planetary Science Letters*, **391**, 183–192.

Gerya, T.V., Stern, R.J., Baes, M., Sobolev, S.V. & Whattam, S.A. 2015. Plate tectonics on the Earth triggered by plume-induced subduction initiation. *Nature*, **527**, 221–225.

Glebovsky, V.Y., Likhachev, A.A., Minakov, A.N., Poselov, V.A., Brekke, H., Ingen, Ø. & Faleide, J.I. 2006*a*. Regional distribution of sedimentary cover in the Nansen Basin based on magnetic data. *In*: Avetisov, G.P. (ed.) *Geological and Geophysical Characteristics of the Lithosphere of the Arctic Region*. Vol. **6**. VNIIOkeangeologia, St Petersburg, 188–193 [in Russian].

Glebovsky, V.Y., Kaminsky, V.D., Minakov, A.N., Merkur'ev, S.A., Childers, V.A. & Brozena, J.M. 2006*b*. Formation of the Eurasia Basin in the Arctic Ocean as inferred from geohistorical analysis of the anomalous magnetic field. *Geotectonics*, **40**, 263–281.

Grantz, A., Clark, D.L. *et al*. 1998. Phanerozoic stratigraphy of Northwind Ridge, magnetic anomalies in the Canada basin, and the geometry and timing of rifting in the Amerasia basin, Arctic Ocean. *Geological Society of America Bulletin*, **110**, 801–820.

Grantz, A., Hart, P.E. & Childers, V.A. 2011. Geology and tectonic development of the Amerasia and Canada Basins, Arctic Ocean. *In*: Spencer, A.M., Embry, A.F., Gautier, D.L., Stoupakova, A.V. & Sørensen, K. (eds) *Arctic Petroleum Geology*. Geological Society, London, Memoirs, **35**, 771–799.

Grogan, P., Østvedt-Ghazi, A.M., Larssen, G.B., Fotland, B., Nyberg, K., Dahlgren, S. & Eidvin, T. 1999. Structural elements and petroleum geology of the Norwegian sector of the northern Barents Sea. *In*: Fleet, A.G. & Boldy, S.A.R. (eds) *Petroleum Geology of Northwest Europe: Proceedings of the 5th Conference*. Geological Society, London, 247–259.

Grogan, P., Nyberg, K., Fotland, B., Myklebust, R., Dahlgren, S. & Riis, F. 2000. Cretaceous magmatism south and east of Svalbard: evidence from seismic reflection and magnetic data. *Polarforschung*, **68**, 25–34.

Grosfils, E.B., McGovern, P.J., Gregg, P.M., Galgana, G.A., Hurwitz, D.M., Long, S.M. & Chestler, S.R. 2013. Elastic models of magma reservoir mechanics: a key tool for investigating planetary volcanism. *In*: Platz, T., Massironi, M., Byrne, P.K. & Hiesinger, H. (eds) *Volcanism and Tectonism Across the Inner Solar System*. Geological Society, London, Special Publications, **401**, 239–267.

Hames, W.E., Renne, P.R. & Ruppel, C. 2000. New evidence for geologically instantaneous emplacement of earliest Jurassic Central Atlantic magmatic province

basalts on the North American margin. *Geology*, **28**, 859–862.

Henriksen, E., Bjørnseth, H.M. *et al.* 2011. Uplift and erosion of the greater Barents Sea: impact on prospectivity and petroleum systems. *In*: Spencer, A.M., Embry, A.F., Gautier, D.L., Stoupakova, A.V. & Sørensen, K. (eds) *Arctic Petroleum Geology*. Geological Society, London, Memoirs, **35**, 271–281.

Hirth, G. & Tullis, J. 1994. The brittle–plastic transition in experimentally deformed quartz aggregates. *Journal of Geophysical Research: Solid Earth*, **99**, 11731–11747.

Hobro, J. 1999. *Three-dimensional tomographic inversion of combined reflection and refraction seismic traveltime data*. PhD thesis, University of Cambridge, Cambridge, Churchill College, UK.

Hobro, J.W., Singh, S.C. & Minshull, T.A. 2003. Three-dimensional tomographic inversion of combined reflection and refraction seismic traveltime data. *Geophysical Journal International*, **152**, 79–93.

Holtzman, B.K., Groebner, N.J., Zimmerman, M.E., Ginsberg, S.B. & Kohlstedt, D.L. 2003. Stress-driven melt segregation in partially molten rocks. *Geochemistry, Geophysics, Geosystems*, **4**, 8607, https://doi.org/10.1029/2001GC000258

Hou, G., Kusky, T.M., Wang, C. & Wang, Y. 2010. Mechanics of the giant radiating Mackenzie dyke swarm: a paleostress field modeling. *Journal of Geophysical Research: Solid Earth*, **115**, B02402.

Ivanova, N.M., Sakulina, T.S., Belyaev, I.V., Matveev, Y.I. & Roslov, Y.V. 2011. Depth model of the Barents and Kara seas according to geophysical surveys results. *In*: Spencer, A.M., Embry, A.F., Gautier, D.L., Stoupakova, A.V. & Sørensen, K. (eds) *Arctic Petroleum Geology*. Geological Society, London, Memoirs, **35**, 209–221.

Jakobsson, M., Mayer, L.A. *et al.* 2012. The International Bathymetric Chart of the Arctic Ocean (IBCAO) Version 3.0. *Geophysical Research Letters*, https://doi.org/10.1029/2012GL052219

Jerram, D.A. & Widdowson, M. 2005. The anatomy of continental flood basalt provinces: geological constraints on the processes and products of flood volcanism. *Lithos*, **79**, 385–405.

Katz, R.F., Spiegelman, M. & Holtzman, B. 2006. The dynamics of melt and shear localization in partially molten aggregates. *Nature*, **442**, 676–679.

Keller, T., May, D.A. & Kaus, B.J. 2013. Numerical modelling of magma dynamics coupled to tectonic deformation of lithosphere and crust. *Geophysical Journal International*, **195**, 1406–1442.

Kendall, J.M., Stuart, G.W., Ebinger, C.J., Bastow, I.D. & Keir, D. 2005. Magma-assisted rifting in Ethiopia. *Nature*, **433**, 146–148.

Khlebnikov, P.A., Belenky, V.Y., Peshkova, I.N., Kazanin, G.S., Shkarubo, S.I., Pavlov, S.P. & Shlykova, V.V. 2011. Geological structure and petroleum potential of the eastern flank of the Northern Barents Basin. *In*: Spencer, A.M., Embry, A.F., Gautier, D.L., Stoupakova, A.V. & Sørensen, K. (eds) *Arctic Petroleum Geology*. Geological Society, London, Memoirs, **35**, 261–269.

Klitzke, P., Faleide, J.I., Scheck-Wenderoth, M. & Sippel, J. 2015. A lithosphere-scale structural model of the Barents Sea and Kara Sea region. *Solid Earth*, **6**, 153–172, https://doi.org/10.5194/se-6-153-2015

Lawver, L.A. & Müller, R.D. 1994. Iceland hotspot track. *Geology*, **22**, 311–314.

Lawver, L.A., Grantz, A. & Gahagan, L.M. 2002. Plate kinematic evolution of the present Arctic region since the Ordovician. *In*: Miller, E.L., Grantz, A. & Klemperer, S.L. (eds) *Tectonic Evolution of the Bering Shelf-Chukchi Sea-Artic Margin and Adjacent Landmasses*. Geological Society of America, Special Papers, **360**, 333–358.

Leever, K.A., Gabrielsen, R.H., Faleide, J.I. & Braathen, A. 2011. A transpressional origin for the West Spitsbergen fold-and-thrust belt: insight from analog modeling. *Tectonics*, **30**, TC2014, https://doi.org/10.1029/2010TC002753

Leith, T.L., Weiss, H.M. *et al.* 1992. Mesozoic hydrocarbon source-rocks of the Arctic region. *In*: Vorren, T.O., Bergsager, E., Dahl-Stamnes, Ø.A., Holter, E., Johansen, B., Lie, E. & Lund, T.B. (eds) *Arctic Geology and Petroleum Potential*. Norwegian Petroleum Society, Special Publication, **2**, 1–25.

Lister, J.R. & Kerr, R.C. 1991. Fluid-mechanical models of crack propagation and their application to magma transport in dykes. *Journal of Geophysical Research: Solid Earth*, **96**, 10049–10077.

Maher, H.D., Jr, 2001. Manifestations of the Cretaceous high Arctic large igneous province in Svalbard. *The Journal of Geology*, **109**, 91–104.

Marello, L., Ebbing, J. & Gernigon, L. 2013. Basement inhomogeneities and crustal setting in the Barents Sea from a combined 3D gravity and magnetic model. *Geophysical Journal International*, https://doi.org/10.1093/gji/ggt018

McHone, J.G., Anderson, D.L., Beutel, E.K. & Fialko, Y.A. 2005. Giant dikes, rifts, flood basalts, and plate tectonics: a contention of mantle models. *In*: Foulger, G.R., Natland, J.H., Presnall, G.C. & Anderson, D.L. (eds) *Plates, Plumes and Paradigms*. Geological Society of America, Special Papers, **388**, 401–420.

McKenzie, D., McKenzie, J.M. & Saunders, R.S. 1992. Dike emplacement on Venus and on Earth. *Journal of Geophysical Research: Planets*, **97**, 15977–15990.

Midtkandal, I. & Nystuen, J.P. 2009. Depositional architecture of a low-gradient ramp shelf in an epicontinental sea: the lower Cretaceous of Svalbard. *Basin Research*, **21**, 655–675.

Midtkandal, I., Faleide, J.I. *et al.* 2015. Source-to-sink dynamics in the Early Cretaceous Boreal Basin; progradational lobes from a missing source. Paper presented at the *AGU Fall Meeting*, San Francisco, CA, USA, 14–18 December 2015. https://agu.confex.com/agu/fm15/webprogram/Paper77221.html

Minakov, A., Mjelde, R., Faleide, J.I., Flueh, E.R., Dannowski, A. & Keers, H. 2012*a*. Mafic intrusions east of Svalbard imaged by active-source seismic tomography. *Tectonophysics*, **518**, 106–118.

Minakov, A., Faleide, J.I., Glebovsky, V.Y. & Mjelde, R. 2012*b*. Structure and evolution of the northern Barents–Kara Sea continental margin from integrated analysis of potential fields, bathymetry and sparse seismic data. *Geophysical Journal International*, **188**, 79–102.

Minshull, T.A., Lane, C.I., Collier, J.S. & Whitmarsh, R.B. 2008. The relationship between rifting and magmatism in the northeastern Arabian Sea. *Nature Geoscience*, **1**, 463–467.

Muller, O.H. & Pollard, D.D. 1977. The stress state near Spanish Peaks, Colorado determined from a dike pattern. *Pure and Applied Geophysics*, **115**, 69–86.

Muskhelishvili, N.I. 1953. *Some Basic Problems of the Mathematical Theory of Elasticity*. Noordhoff International Publishing, Groningen.

Nejbert, K., Krajewski, K.P., Dubińska, E. & Pécskay, Z. 2011. Dolerites of Svalbard, north-west Barents Sea Shelf: age, tectonic setting and significance for geotectonic interpretation of the High-Arctic large igneous province. *Polar Research*, **30**, 7306, https://doi.org/10.3402/polar.v30i0.7306

Nielsen, T.K. & Hopper, J.R. 2004. From rift to drift: mantle melting during continental breakup. *Geochemistry, Geophysics, Geosystems*, **5**, Q07003, https://doi.org/10.1029/2003GC000662

Ntaflos, T. & Richter, W. 2003. Geochemical constraints on the origin of the continental flood basalt magmatism in Franz Josef Land, Arctic Russia. *European Journal of Mineralogy*, **15**, 649–663.

Odé, H. 1957. Mechanical analysis of the dike pattern of the Spanish Peaks area, Colorado. *Geological Society of America Bulletin*, **68**, 567–576.

Olesen, O., Brönner, M. *et al.* 2010. New aeromagnetic and gravity compilations from Norway and adjacent areas: methods and applications. *In*: Vining, B.A. & Pickering, S.C. (eds) *Petroleum Geology: From Mature Basins to New Frontiers – Proceedings of the 7th Petroleum Geology Conference*. Geological Society, London, 559–586.

Paige, C.C. & Saunders, M.A. 1982. LSQR: an algorithm for sparse linear equations and sparse least squares. *ACM Transactions on Mathematical Software*, **8**, 43–71.

Papamichos, E., Tronvoll, J., Skjærstein, A. & Unander, T.E. 2010. Hole stability of red Wildmoor sandstone under anisotropic stresses and sand production criterion. *Journal of Petroleum Science and Engineering*, **72**, 78–92.

Piepjohn, K., Gosen, W.V., Estrada, S. & Tessensohn, F. 2007. Deciphering superimposed Ellesmerian and Eurekan deformation, Piper Pass area, northern Ellesmere Island (Nunavut). *Canadian Journal of Earth Sciences*, **44**, 1439–1452.

Piskarev, A.L., Heunemann, C., Makar'ev, A.A., Makar'eva, A.M., Bachtadse, V. & Aleksyutin, M. 2009. Magnetic parameters and variations in the composition of igneous rocks of the Franz Josef Land archipelago. *Izvestiya, Physics of the Solid Earth*, **45**, 150–166.

Pollard, D.D. 1973. Derivation and evaluation of a mechanical model for sheet intrusions. *Tectonophysics*, **19**, 233–269.

Polteau, S., Hendriks, B.W. *et al.* 2016. The Early Cretaceous Barents Sea Sill Complex: Distribution, $^{40}Ar/^{39}Ar$ geochronology, and implications for carbon gas formation. *Palaeogeography, Palaeoclimatology, Palaeoecology*, **441**, 83–95.

Regenauer-Lieb, K. 1998. Dilatant plasticity applied to Alpine collision: ductile void growth in the intraplate area beneath the Eifel volcanic field. *Journal of Geodynamics*, **27**, 1–21.

Regenauer-Lieb, K. & Petit, J.P. 1997. Cutting of the European continental lithosphere: plasticity theory applied to the present Alpine collision. *Journal of Geophysical Research*, **102**, 7731–7746.

Richards, M.A., Duncan, R.A. & Courtillot, V.E. 1989. Flood basalts and hot-spot tracks: plume heads and tails. *Science*, **246**, 103–107.

Ridley, V.A. & Richards, M.A. 2010. Deep crustal structure beneath large igneous provinces and the petrologic evolution of flood basalts. *Geochemistry, Geophysics, Geosystems*, **11**, Q09006, https://doi.org/10.1029/2009GC002935

Ritzmann, O. & Faleide, J.I. 2007. Caledonian basement of the western Barents Sea. *Tectonics*, **26**, TC5014, https://doi.org/10.1029/2006TC002059

Rozhko, A.Y., Podladchikov, Y.Y. & Renard, F. 2007. Failure patterns caused by localized rise in pore-fluid overpressure and effective strength of rocks. *Geophysical Research Letters*, **34**, L22304, https://doi.org/10.1029/2007GL031696

Rudnicki, J.W. & Rice, J.R. 1975. Conditions for the localization of deformation in pressure-sensitive dilatant materials. *Journal of the Mechanics and Physics of Solids*, **23**, 371–394.

Sakoulina, T.S., Pavlenkova, G.A. & Kashubin, S.N. 2015. Structure of the Earth's crust in the northern part of the Barents–Kara region along the 4-AR DSS profile. *Russian Geology and Geophysics*, **56**, 1622–1633.

Sato, H., Fehler, M.C. & Maeda, T. 2012. *Seismic Wave Propagation and Scattering in the Heterogeneous Earth*. Springer, Berlin.

Smith, W.H.F. & Sandwell, D.T. 1997. Global seafloor topography from satellite altimetry and ship depth soundings. *Science*, **277**, 1957–1962.

Senger, K., Tveranger, J., Ogata, K., Braathen, A. & Planke, S. 2014*a*. Late Mesozoic magmatism in Svalbard: a review. *Earth-Science Reviews*, **139**, 123–144.

Senger, K., Planke, S., Polteau, S., Ogata, K. & Svensen, H. 2014*b*. Sill emplacement and contact metamorphism in a siliciclastic reservoir on Svalbard, Arctic Norway. *Norwegian Journal of Geology*, **94**, 155–169.

Shephard, G.E., Müller, R.D. & Seton, M. 2013. The tectonic evolution of the Arctic since Pangea breakup: integrating constraints from surface geology and geophysics with mantle structure. *Earth-Science Reviews*, **124**, 148–183.

Shipilov, E.V. & Karyakin, Y.V. 2011. The Barents Sea magmatic province: geological–geophysical evidence and new $^{40}Ar/^{39}Ar$ dates. *Doklady Earth Sciences*, **439**, 955–960.

Sigmundsson, F., Hooper, A. *et al.* 2015. Segmented lateral dyke growth in a rifting event at Bárðarbunga volcanic system, Iceland. *Nature*, **517**, 191–195.

Skilbrei, J.R. 1991. Interpretation of depth to the magnetic basement in the northern Barents Sea (south of Svalbard). *Tectonophysics*, **200**, 127–141.

Skilbrei, J.R. 1992. Preliminary interpretation of aeromagnetic data from Spitsbergen, Svalbard Archipelago (76–79 N): implications for structure of the basement. *Marine Geology*, **106**, 53–68.

Smelror, M., Petrov, O.V., Larssen, G.B. & Werner, S.C. 2009. *Geological History of the Barents Sea*. Norges Geologiske Undersøkelse, Trondheim.

Svensen, H., Corfu, F., Polteau, S., Hammer, Ø. & Planke, S. 2012. Rapid magma emplacement in the Karoo large igneous province. *Earth and Planetary Science Letters*, **325**, 1–9.

Sweeney, J.F. 1985. Comments about the age of the Canada Basin. *Tectonophysics*, **114**, 1–10.

Tapponnier, P. & Molnar, P. 1976. Slip-line field theory and large-scale continental tectonics. *Nature*, **264**, 319–324.

Tarduno, J.A. 1998. The high Arctic large igneous province. Paper presented at the *Third International Conference on Arctic Margins (ICAM-III)*, 12–15 October 1998, Federal Institute of Geoscience and Natural Resources, Celle, Germany.

Tegner, C. & Pease, V. 2014. Continental flood basalts of Bennett Island, East Siberian Sea: high Arctic geodynamics. Paper presented at the *16th EGU General Assembly 2014*, 27 April–2 May, Vienna, Austria, Geophysical Research Abstracts, Vol. **16**, EGU2014-2452, http://meetingorganizer.copernicus.org/EGU2014/EGU2014-2452.pdf

Tegner, C., Storey, M., Holm, P.M., Thorarinsson, S.B., Zhao, X., Lo, C.H. & Knudsen, M.F. 2011. Magmatism and Eurekan deformation in the High Arctic large igneous province: $^{40}Ar-^{39}Ar$ age of Kap Washington Group volcanics, North Greenland. *Earth and Planetary Science Letters*, **303**, 203–214.

Thórarinsson, S.B., Söderlund, U., Døssing, A., Holm, P.M., Ernst, R.E. & Tegner, C. 2015. Rift magmatism on the Eurasia basin margin: U–Pb baddeleyite ages of alkaline dyke swarms in North Greenland. *Journal of the Geological Society*, **172**, 721–726.

Vardoulakis, I., Sulem, J. & Guenot, A. 1988. Borehole instabilities as bifurcation phenomena. *International Journal of Rock Mechanics and Mining Sciences & Geomechanics Abstracts*, **25**, 159–170.

Verba, V.V., Astafurova, E.G., Leonov, V.O., Mandrikov, V.S. & Chlupin, N.I. 2004. Structure of the Northern Continental Margin of the Barents Sea Shelf (in Environments of Franz Joseph Land). *Geological–Geophysical Features of the Lithosphere of the Arctic Region*, **5**. VNIIOkeangeologia, St Petersburg.

Vermeer, P.A. & de Borst, R. 1984. Non-associated plasticity for soils, concrete and rock. *HERON*, **29**, 1984.

Weinberg, R.F. & Regenauer-Lieb, K. 2010. Ductile fractures and magma migration from source. *Geology*, **38**, 363–366.

White, R.S. & McKenzie, D. 1995. Mantle plumes and flood basalts. *Journal of Geophysical Research: Solid Earth*, **100**, 17543–17585.

White, R.S., Drew, J., Martens, H.R., Key, J., Soosalu, H. & Jakobsdóttir, S.S. 2011. Dynamics of dyke intrusion in the mid-crust of Iceland. *Earth and Planetary Science Letters*, **304**, 300–312.

Yarushina, V.M. & Podladchikov, Y.Y. 2007. The effect of nonhydrostaticity on elastoplastic compaction and decompaction. *Izvestiya, Physics of the Solid Earth*, **43**, 67–74.

Yarushina, V.M., Dabrowski, M. & Podladchikov, Y.Y. 2010. An analytical benchmark with combined pressure and shear loading for elastoplastic numerical models. *Geochemistry, Geophysics, Geosystems*, **11**, Q08006, https://doi.org/10.1029/2010GC003130

Yarushina, V.M., Podladchikov, Y.Y. & Connolly, J.A. 2015. (De)compaction of porous viscoelastoplastic media: solitary porosity waves. *Journal of Geophysical Research: Solid Earth*, **120**, 4843–4862.

Yu, H.S. 2007. *Plasticity and Geotechnics*. Springer Science & Business Media, Heidelberg.

Zienkiewicz, O.C. & Taylor, R.L. 2005. *The Finite Element Method for Solid and Structural Mechanics*. Butterworth-Heinemann, Oxford.